COMPUTER-AUTOMATED SHADOW MOIRÉ METHOD AND APPLICATIONS FOR 3D SURFACE PROFILING

by

Rui Zhao

Bachelor of Science in Mechanical Engineering

Beijing University of Aeronautics and Astronautics, July 1998

A Thesis presented to Ryerson University in partial fulfillment of the requirements for the Degree of Master of Applied Science in the program of Mechanical Engineering

Toronto, Ontario, Canada, 2006

DECLARATION

I hereby declare that I am the sole author of this project.

I authorize Ryerson University to lend this thesis to other institutions or individuals for the purpose of scholarly research.

Rui Zhao

I further authorize Ryerson University to reproduce this report by photocopying or by other means, in total or in part, at the request of other institutions or individuals for the purpose of scholarly research.

Rui Zhao

PUBLICATIONS AND PRESENTATIONS

Publications:

1. R. Zhao, H. Lu, M. Zhou, C. Sun, "Surface Profiling Using a Modified Shadow Moiré Technique," IEEE, *International Symposium and Exhibition on Advanced Packaging Materials* , pp.151-154 (2006)

2. R. Zhao, H. Lu, M. Zhou, C. Sun, "Improved Shadow Moiré Method for Out-of-plane Displacement Measurement," Canadian Society for Mechanical Engineering (2006)

3. C. Sun, J. Chen, R. Zhao and H. Lu, "A New Phase Analysis Algorithm for LC Cell Implemented Digital Special Shearography," Canadian Society for Mechanical Engineering (2006)

Conference presentations:

1. "Surface Profiling Using a Modified Shadow Moiré Technique," International Symposium and Exhibition on Advanced Packaging Materials, Atlanta, USA, March, 15 - 17, 2006.

2. "Improved Shadow Moiré Method for Out-of-plane Displacement Measurement," CSME (Canadian Society for Mechanical Engineering) Forum, Calgary, Alberta, May, 21 - 24, 2006.

ABSTRACT

Computer-automated Shadow Moiré Method and Applications for 3D Surface Profiling

© Rui Zhao, 2006
Master of Applied Science
in the program of
Mechanical Engineering
Ryerson University

Among numerous methods for 3D surface profiling, classic shadow moiré method has been kept as the most popular one due to its full-field feature and low cost. This thesis focuses on a computer-vision shadow moiré method with a scope to improve the measurement resolution, accuracy and efficiency. The computer automation is basically realized through the introduction of a phase-shifting technique that is incorporated with a new multi-grid least-square unwrapping algorithm. The method is enhanced by implementing a few additional image processing techniques. These techniques, when implemented, result in improved measurement accuracy and enable easy applications to irregularly shaped surfaces. The study also proposes a new, automated system calibration approach that is based on a real-time image subtraction. A data normalization process is studied to resolve possible confusions in the presentation of the original data. The verification test results show that the modified shadow moiré technique has achieved the initial goal, in that the measurement resolution now reaches a few percentage of the fringe sensitivity.

ACKNOWLEDGEMENTS

First of all, I would like to express my sincere gratitude to Professor Hua Lu for his continuous academic support and valuable guidance during my studies at Ryerson. I have learned a tremendous amount under his supervision. I also appreciate the help from Ms. Ming Zhou, who provide technical support to me throughout the experimental testing. Finally, I would like to thank my friends here. Without them, I would not have had the pleasant and memorable time.

DEDICATION

To my parents and my sister for their unfailing support and encouragement in this endeavor.

TABLE OF CONTENTS

ABSTRACT vii

ACKNOWLEDGEMENTS ix

DEDICATION xi

LIST OF FIGURES xv

LIST OF TABLES xix

NOMENCLATURE xxi

CHAPTER 1 INTRODUCTION 1

1.1 Moiré Phenomenon 1

1.2 Moiré fringe interpretations 3

1.3 Moiré in engineering 10

1.4 Background and objectives of current research 11

CHAPTER 2 SHADOW MOIRÉ BASICS AND COMPUTER AUTOMATION 15

2.1 Shadow moiré fringe formation and interpretation 16

2.2 History of shadow moiré and computer fringe processing 20

2.3 Phase-shifting techniques implemented to shadow moiré 21

2.4 Phase unwrapping 27

2.4.1 Least-square phase unwrapping algorithms 29

2.4.2 Multi-Grid phase unwrapping algorithm 30

2.4.3 Comparison of Phase Unwrapping Methods 32

2.5 Computer-automated shadow moiré system realization 33

CHAPTER 3 IMAGE PROCESSING TECHNIQUES APPLIED TO SHAODW MOIRE 36

3.1 Noise reduction from phase diagrams 36

3.1.1 Noise in digital images 36

3.1.2 Noise affected phase diagram and treatment 37

3.1.3 Noise reduction filters 40

3.2 Differentiate object from background by image segmentation 45

3.2.1 Boundary extraction techniques 45

3.2.2 Outer boundary tracing 50

3.2.3 Image segmentation 52

3.3 System calibration by image subtraction and grey-scale histogram 54

CHAPTER 4 SHADOW MOIRÉ DATA PRESENTAION **58**

4.1 Need of new reference plane in data presentation 58

4.2 Reference plane determined by three corners of the surface 60

4.3 Best fit plane 63

4.4 Comparison of two reference methods 66

CHAPTER 5 VERIFICATION AND APPLICATIONS OF THE NEW SHADOW MOIRÉ TECHNIQUE **67**

5.1 Verification tests 67

5.2 A typical application to microelectronics 69

5.3 Error analysis 76

CHAPTER 6 CONCLUSIONS **78**

REFERENCES **81**

APPENDIX 1 **89**

APPENDIX 2 **93**

LIST OF FIGURES

1.1 A line grating composed of straight and parallel lines 2

1.2 Moiré fringes generated by superimposing two similar line gratings [15] 2

1.3 Moiré pattern obtained by superimposing two circular line gratings [5] 3

1.4 Geometric moiré in the case of rotation 6

1.5 Geometric moiré in the case of pure elongation 7

1.6 Schematic diagram of projection moiré setup [14] 10

2.1 Shadow Moiré Fringe pattern induced by Interference 15

2.2 Geometry of shadow moiré 17

2.3 Shadow moiré with configuration of normal viewing [16] 19

2.4 Fringe movement related to grating translation 22

2.5 Fringe patterns obtained in phase shifting method and result contours 27

2.6 Plot of true phase and wrapped phase 28

2.7 Multigrid algorithm using Restriction and Prolongation operations 31

2.8 Experimental setup of shadow moiré method 35

2.9 Three-dimensional, 6-axis micro-motion stage with glass grating 35

3.1 (a) Phase diagram of an antenna corrupted by noise (b) Phase diagram with less noise after using proposed scheme (c) Phase diagram after 5x5 Median filtering 39

3.2 A 3x3 neighbourhood around a point (x,y) in an image 41

3.3 (a) Lena image with Gaussian noise [53]

(b) Image after 3x3 averaging filtering 42

3.4 (a) Lena image with Salt and Pepper noise

(b) Image after 3x3 averaging filtering 42

3.5 (a) Lena image with Salt and Pepper noise [53]

(b) Image after 3x3 Median filtering 44

3.6 (a) Lena image with Gaussian noise [53]

(b) Image after 3x3 Median filtering 44

3.7 Dilation of A by structuring element B 46

3.8 Erosion of A by structuring element B 47

3.9 (a) A simple binary image (b) Extracted boundaries using Eq.3.8 48

3.10 Warpage measurement for an antenna structure: (a) image with moiré fringes

(b) noise-free phase diagram (c) detected inner and outer boundaries

(d) 2-D surface warpage contour map (e) 3-D plot of warpage after

background removed (f) 3-D surface warpage plotted with background 49

3.11 Moore Neighbour 50

3.12 Outer boundary tracing scheme 51

3.13 (a) A simple binary image (b) Outer contour detected by Moore-Neighbour

tracing technique 52

3.14 Surface topography of a Canadian quarter-coin measured by phase shifted

shadow moiré: (a) a typical 4-step phase shifted image; (b) phase diagram

with background; (c) phase diagram with background removed;

(d) 2-D surface contours; (e) 3-D surface topography plot with no background;

(f) 3-D plot without applying boundary detection 53

3.15 Conventional system calibration scheme 55

3.16 Determination of system sensitivity by a real-time image subtraction scheme:

(a) an original fringe pattern; (b) an artificial image of subtraction of the fringe pattern with π phase shift from the original pattern; (c) subtraction of the fringe pattern with π/2 phase shift from the original pattern; (d) subtraction of the fringe pattern with 2π phase shift from the original pattern. A curve of the histogram is also shown in each image 57

4.1 Two-Dimensional data normalization to eliminate effect of rigid body motion.... 59

4.2 New reference plane determined by three corner points of the surface being measured 60

4.3 (a) Surface profile before 3-point plane normalization (b) Surface profile after 3-point plane normalization 62

4.4 Least-Square best fitting for straight line 63

4.5 (a) Surface profile before best-fit plane normalization (b) Surface profile after best-fit plane normalization 65

5.1 Experimental results for gage block measurement (a) Schematic plot of a gage block (b) Gage block image with moiré pattern (c) 3-D surface profile 68

5.2 Schematic diagram of BGA and PCB assembly 69

5.3 BGA temperature vs. time 70

5.4 Warpage of BGA and PWB at different temperature 72

5.5 Warpage of BGA and PWB during the reflow process 75

5.6 Analysis of shadow moiré measurement error caused by using a point light source 77

A-1 Program flow chart of the modified shadow moiré technique 89

A-2 (a) Warpage of a PBGA at room temperature..... 93

A-2 (b) Warpage of a PCBA at room temperature..... 93

A-2 (c) Warpage of a CBGA at room temperature..... 94

LIST OF TABLES

5.1 Shadow moiré result compared to that measured by Micro caliper 69

NOMENCLATURE

Roman	Description
A	An image set
$A(x,y)$	Background intensity
a	Constant
B	Structuring element
B_x	Translation of B by x
$B(x,y)$	Moiré fringe amplitude
b	Constant
c	Constant
$c_{i,j}$	Coarse grid
D	Distance between light source and camera
E	Least square error
$f_{i,j}$	Fine grid
$f(x,y)$	Noise-corrupted image
$g(x,y)$	Noise-free image
$I_i(x,y)$	Intensity distribution function of moiré fringes (i = 0, 1, 2, 3, 4)
i, j	Pixel numbering in x and y direction respectively
$k(x,y)$	An integer
L	Distance between light source and sample
M	Width of the phase array
N	Height of the phase array
$N(x,y)$	Fringe order

p_1	Pitch of reference (master) grating
p_1	Pitch of specimen grating
$p(x)$	Gaussian distribution function
r	Constant
v(x,y)	Noise distribution function
W(x,y)	Distance between a point on the surface and glass grating surface
w	System sensitivity
z	Function of a plane

Greek	**Description**
α	Angle between reference grating and moiré fringe
θ	Angle between reference grating and specimen grating
δ	Pitch of the moiré fringes
$\phi(x,y)$	Phase of moiré fringe
π	Pi = 3.1415926
$\phi(x,y)$	Wrapped phase
$\Phi(x,y)$	Unwrapped phase
$\Delta_{i,j}^{x}$	Partial derivatives of wrapped phase along x axis
$\Delta_{i,j}^{y}$	Partial derivatives of wrapped phase along y *axis*
μ	Mean deviation of the random variable
σ	Standard deviation of the random variable
β(A)	Boundary of image A

CHAPTER 1 INTRODUCTION

1.1 Moiré phenomenon

The word *moiré* originates from the French language referring to wave-like patterns. The moiré effect is an optical phenomenon that is visible when two or more periodically structured patterns (such as line gratings and screens, etc.) are superimposed [1]. Though certain such phenomena have adverse effects, such as the aliasing phenomenon seen in TV, film and video displays and signal transfers, moiré has found significant applications in areas related to metrology, especially for surface shape and deformation measurement.

A line grating usually comprises alternately varying opaque and transparent lines that are equally distanced, as seen in Fig 1.1. The distance between two adjacent lines is constant and called the *pitch*, and the number of grating lines per unit length is referred to as the *density* of the grating. The superposition of two similar gratings can produce a moiré pattern with bright and dark fringes referred to as *moiré fringes*. The following discussed cases each involves a pair of such gratings, of which the one that keeps the pitch and the orientation unchanged is called the *master grating* or *reference grating*, and the other that is adhered to a specimen and therefore its pitch and orientation change as the specimen deforms is defined as the *specimen grating*.

Fig. 1.2 shows a moiré fringe pattern generated by two identical line gratings that are rotated by a small angle with respect to each other. As the angle increases, the distance between any two adjacent dark fringes decreases. The moiré fringes so generated are

parallel and alternate light and dark bars. They are uniformly spaced over the superimposed grating area. For an arbitrarily deformed specimen subjected to mechanical or thermal loads, the obtained moiré fringes are usually curved and unequally spaced, and the moiré pattern thus carries the information of the specimen deformation.

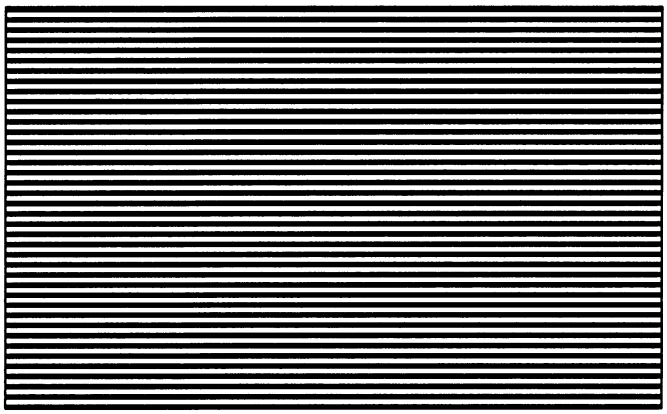

Fig. 1.1 A line grating composed of straight and parallel lines.

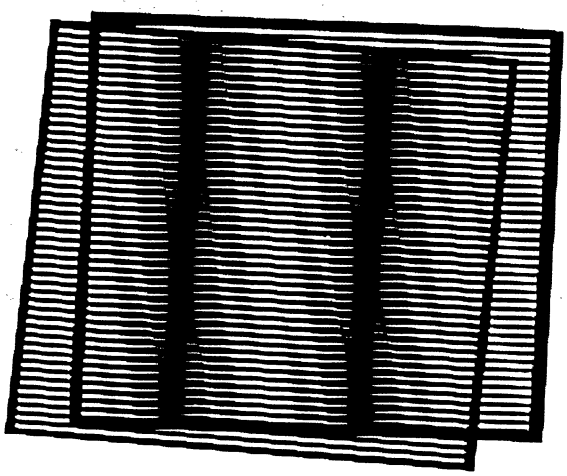

Fig 1.2 Moiré fringes generated by superimposing two similar line gratings. [15]

Curved gratings with circular and radial lines are used in some applications [1-3,5]. One example involves gratings of circular lines. When the specimen grating is deformed to become elliptical, the superposition of the deformed and the reference gratings generates a fringe pattern as typically seen in Fig.1.3. In this case, the fringe pattern reveals the radial component of the specimen displacement.

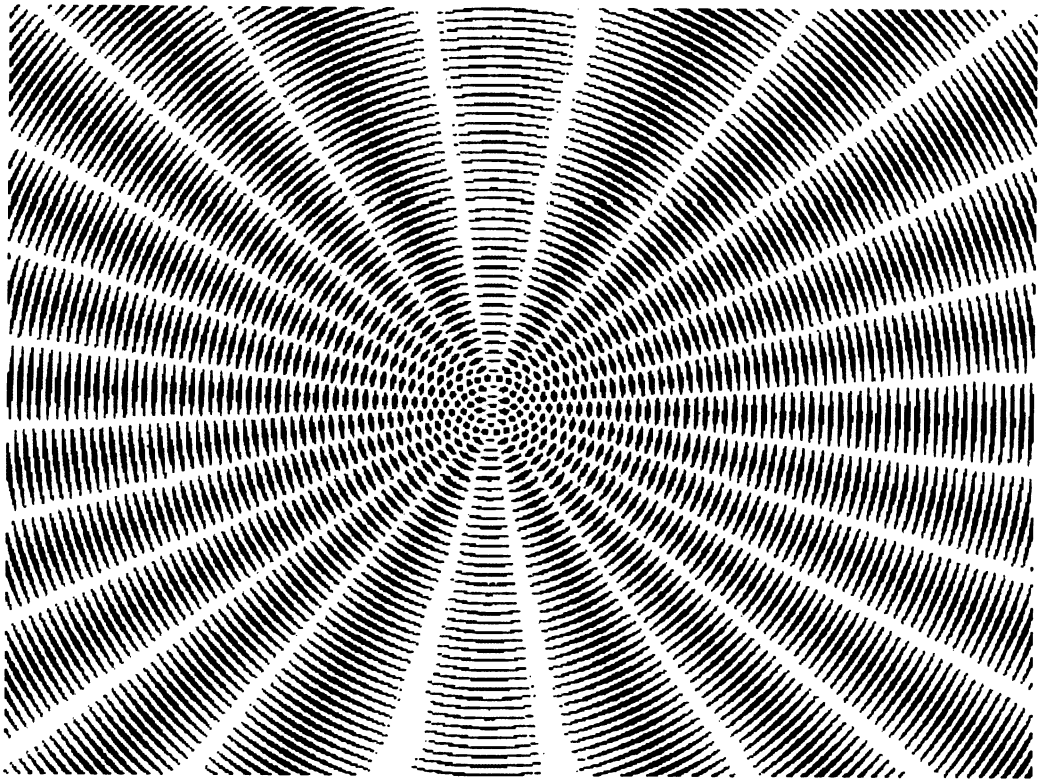

Fig.1.3 Moiré pattern obtained by superimposing two circular line gratings. [5]

1.2 Moiré fringe interpretations

The moiré fringes, representing displacement contours of the specimen, map and visualize the geometric difference (in pitch and orientation) between the pair of master and specimen

gratings. The moiré effect has attracted much interest in metrology related areas of applications, especially in experimental solid mechanics. For the latter, the determination of in-plane and out-of-plane displacement due to the motion and deformation of a surface is of a primary interest. Of the various methods that have been researched, the classic two-dimensional geometric moiré and the laser based moiré interferometry belong to the in-plane methods and the shadow moiré and projection moiré are for the out-of-plane measurement. The fringe interpretation is a key step in applications of these methods.

Classic in-plane geometric moiré

In the history of development of moiré methods, the classic geometric in-plane moiré is the very first to be studied. It is called *geometric moiré* because the mathematical relationship between the properties of grating lines and those of the resulted moiré fringes can be obtained based on a simple geometric analysis [2, 3]. Taking the case of the pure rigid-body rotation as an example in which the specimen grating is rotated by an angle with respect to the reference grating, the analysis is performed based on a schematic shown in Fig.1.4. In the diagram, the two parallel lines A1 and A2, belonging to a specimen grating of pitch p_2, are parallel and adjacent to each other; so are the lines B1, B2 and B3 of the reference grating of pitch p_1; lines C1 and C2 are the center lines of moiré fringes shown as the bars with three lines; θ is the angle of rotation of the specimen grating and α the angle between the reference grating lines and the moiré fringes. A simple geometric analysis yields a mathematical relationship as follows:

$$\frac{p_1}{p_2} = \frac{\sin(\alpha)}{\sin(\alpha+\theta)} \tag{1.1}$$

Equation (1.1) can be used to yield the intersection angle α as:

$$\alpha = \arctan\left[\frac{\sin(\theta)p_2}{p_1 - \cos(\theta)p_2}\right] \tag{1.2}$$

A similar analysis relates the pitch of the specimen grating, p_2, and the moiré fringe spacing, δ, as

$$\frac{\delta}{p_1} = \frac{\sin(\alpha+\theta)}{\sin(\theta)} \tag{1.3}$$

Substituting α in Eq.1.2 to Eq.1.3, fringe spacing δ can be obtained as

$$\delta = \frac{p_2^2}{\sqrt{p_2^2 + p_1^2 - 2p_1p_2\cos(\theta)}} \tag{1.4}$$

Since no deformation occurs in the rigid body rotation case, $p_1 = p_2 = p$ and Eq.1.4 can be rewritten as

$$\delta = \frac{p}{2\sin(\theta/2)} \tag{1.5}$$

Eq.1.5 can be approximately replaced with a simpler form as

$$\delta = \frac{p}{\theta} \tag{1.6}$$

as long as θ is sufficiently small. In another case where the specimen is under simple tensile loading, the specimen grating is so stretched that in the length of δ there is one grating line more than in the reference grating, as shown in Fig. 1.5. Given the specimen grating pitch p_1 and the reference grating pitch p_2, the fringe spacing is related to the pitches by

$$\delta = np_2 = (n+1)p_1 \tag{1.7}$$

where n is the number of grating lines in between the two adjacent fringes in the reference grating. Eliminating n in Eq.1.7 yields the relation between the fringe spacing and the grating pitches as

$$\frac{1}{\delta} = \frac{1}{p_1} - \frac{1}{p_2} \tag{1.8}$$

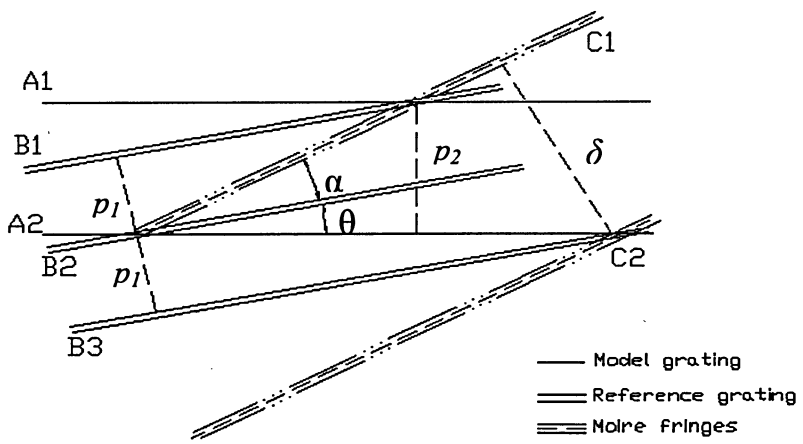

Fig. 1.4 Geometric moiré in the case of rotation.

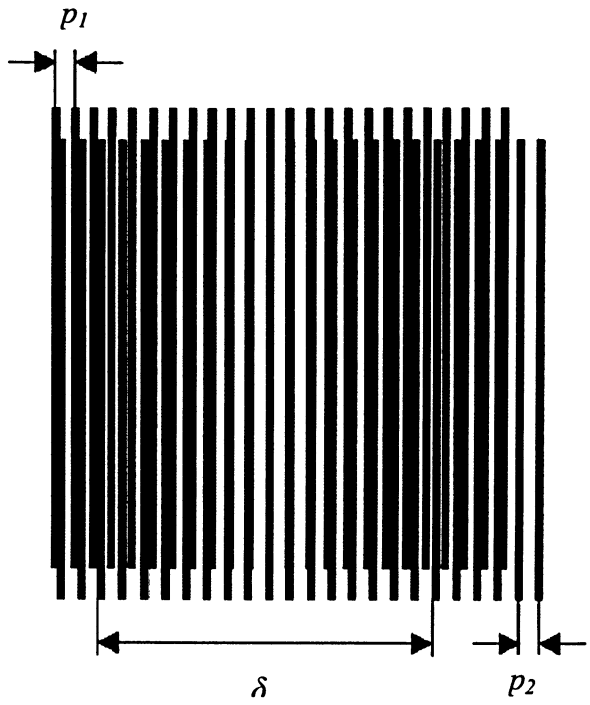

Fig. 1.5 Geometric moiré in the case of pure elongation.

Out-of-plane moiré

Shadow moiré and projection moiré are both commonly applied in measuring three-dimensional deformation of a surface. Displacement is measured by comparing the fringe patterns obtained before and after the object movement or load application has occurred. Shadow moiré [1,2,4,6,7] occurs due to the interference between a reference grating and the shadow of the grating projected onto a surface. The resulted fringe pattern characterizes the distance from a surface point to the reference grating. Due to its low cost and easy-to-apply, shadow moiré becomes very popular for measuring relatively small objects with limited depth range. A brief introduction of projection moiré method is given below, while the shadow moiré method will be discussed in detail in the latter chapters.

The method of projection moiré has the capability of measuring large objects yet at the expense of reduced resolution. Several projection moiré methods similar in principle but differing in implementation have been reported [1,4,5,14, 25,38]. Fig.1.6 shows a schematic of one such configuration. The grating projected onto an object surface becomes distorted in accordance to the surface' topographic features. When both the projected grating and a reference grating are superimposed, a moiré pattern is generated. The moiré fringes map the surface topography as topographic contour lines. Implementing a phase shifting technique can improve the measurement resolution. In such a proposed setup, an electric translator is used to translate the projected grating to realize the phase shifting. With several projected gratings, each translated at a certain amount, a set of phase shifted fringe patterns can be obtained. An analysis for the relationship between the surface warpage and moiré fringe results in the following expression

$$W(x,y) = N(x,y)p/(\tan\alpha + \tan\beta) \qquad (1.9)$$

where α and β are the illumination angle and observation angle, respectively, $N(x,y)$ is the fringe order at a point (x, y), which is not necessarily an integer number, and p is the pitch of the reference grating. Further analysis can show that Eq.1.9 applies to both projection moiré and shadow moiré.

A moiré fringe pattern can be mathematically represented by the variation of light intensity across the pattern as

$$I_i(x,y) = A(x,y) + B(x,y)\cos[\phi(x,y)+(\frac{\pi}{2})k], \qquad k = 0,1,2,3. \qquad (1.10)$$

$\phi(x, y)$ is the phase angle and can be calculated from the following equation

if four of the above mentioned phase-shifted fringe patterns are made available:

$$\phi(x,y) = \arctan[(I_3-I_1)/(I_0-I_2)] \tag{1.11}$$

where I_0, I_1, I_2 *and* I_3 are the intensity distribution functions of such patterns, each having the phase shifted by 0, $\pi/2$, π and $3\pi/2$, respectively. Upon obtaining the phase angle $\phi(x, y)$ at a point, the fringe order $N(x, y)$ of the point can be obtained via

$$N(x, y) = \frac{\phi(x, y)}{2\pi} \tag{1.12}$$

The classic moiré fringe analysis relies on rough estimates of fringe orders merely based on the light intensity. The implementation of computer vision and phase shifting techniques has not only achieved computer automation, but also dramatically increased the accuracy and resolution of the moiré methods.

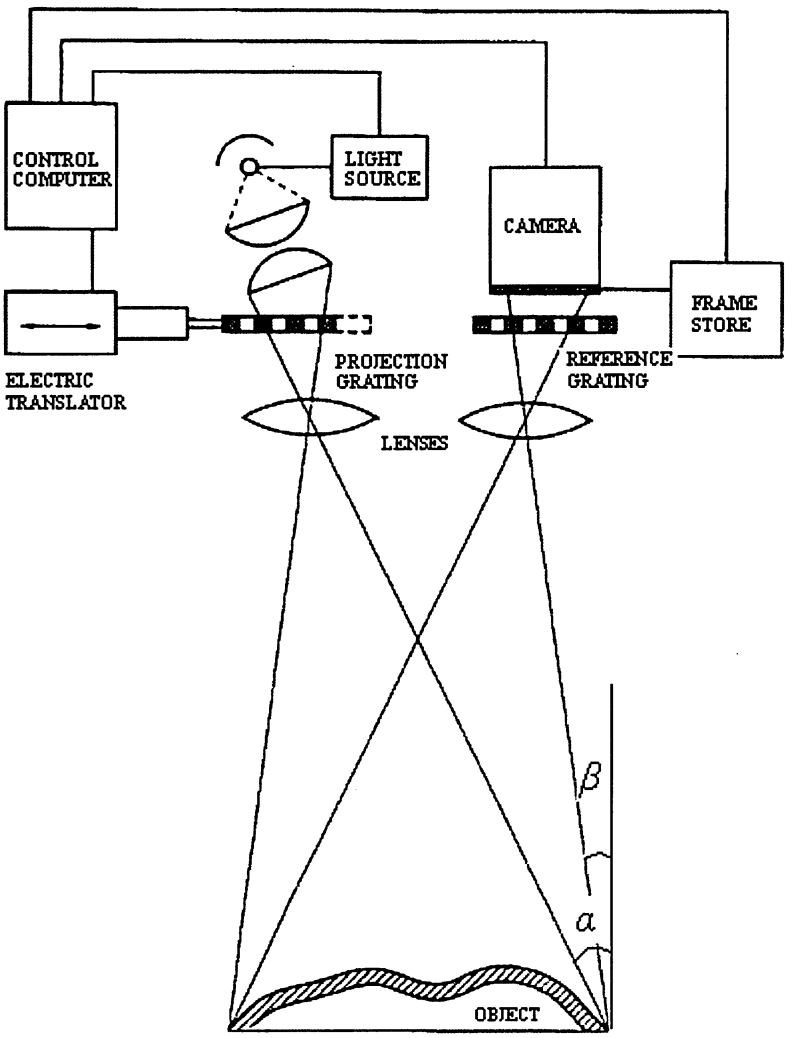

Fig.1.6 Schematic diagram of projection moiré setup. [14]

1.3 Moiré in engineering

The history of the study of moiré phenomena can be tracked back to over a hundred years ago. Lord Rayleigh [31], in 1874, first observed the interference pattern by superimposing two diffraction gratings. Rayleigh proposed an application of using the moiré technique in testing diffraction grids. Mulot in 1925 applied that technique to study the deformation of mica layers. Later in 1945, Tollenar reported that moiré fringes could be used to magnify

displacements, being also suitable as a photoelastic method. Later Weller and Shepherd in 1948 presented another significant advance. They used the moiré technique to measure deformation of an object under applied stress by looking at the differences in a grating pattern that changed due to the stress application. In the 1950's, Ligtenberg and Guild realized moiré interferometry method for stress analysis by mapping slope contours and displacement measurement. It was not until the 1970s that the use of moiré to measure surface topography was first proposed by Meadows [34], Takasaki [35], and Wasowski [36], separately. Digital processing and analysis of moiré fringe pattern, first reported by Yatagai et al [32] in 1982, came only after the computer and CCD (Charge Coupled Device) became popularly available. According to Hu [66] (2003), projection moiré and shadow moiré are to-date the most frequently employed shape surveying techniques due to their simplicity and quickness. The conventional applications include the measurement of surface topography, deformation due to mechanical and thermal loading, and vibration mode analysis, etc. It is only very recently that the high sensitive shadow moiré has found wide applications in electronics industry, in particular in measuring the warpage of microelectronic devices under mechanical and thermal loading.

1.4 Background and objectives of current research

As mentioned, shadow moiré as a practical method has been widely employed for out-of-plane surface profiling and warpage measurement. It is not only until recent years and due to the trend of shifting from failure statistics-based to physics-based reliability assessment, that the shadow moiré method has been brought to the attention of the microelectronics research and manufacturing industry. Applications to measuring thermally induced

warpage for PCBs (printed circuit board), components and assemblies have made possible the quantitative determination of deformation parameters for the packages. The merits of the method including low cost, quick application and higher accuracy and resolution, are largely attributed to the adoption, first in 1990, of the phase-shifting technique. Mainly driven by the demand for higher sensitivity and resolution, Dirckx and Decraemer [33] proposed a system for an automated three-dimensional surface measurement using a four-step phase shifting algorithm. As a computer vision and digital processing method aided by the phase-shifting technique, shadow moiré reaches a measurement sensitivity of better than 2 microns and a much improved spatial resolution that depends both on the optical and video resolutions of the system. Moreover, the direction of the warpage is automatically determined due to the nature of the fringe shifting. Even though the existing shadow moiré techniques are pretty mature with the merits as just described, there are still some limitations and drawbacks that need to be improved.

The research applications have shown that further improvement of the shadow moiré technique is yet much needed in many ways. First, the existing versions of shadow moiré technique commonly adopt the FFT (Fast Fourier Transform) and the DCT (Discrete Cosine Transform) least-square unwrapping algorithms in order to recover the real phase values. These algorithms commonly have restrictions imposed on the size of the wrapped phase data array used in fringe processing, which limits the measurement resolution. Second, the conventional system calibration scheme relies largely on the use of standard shaped surface or gauge blocks and thus requires human operator's experience. When a

system needs to reset-up, uncertainty involved in the system sensitivity calibration is often a concern. Furthermore, conventionally the shadow moiré technique measures a surface profile within prescribed square or rectangular shaped boundaries. Measuring any irregularly shaped surfaces will require a new methodology in processing. Finally, as the method is applied to measuring the deformation induced surface warpage, the changes of a fringe pattern in responding to the surface rigid body motion may cause confusion in interpreting the surface deformation. A proper normalization procedure is needed in order to eliminate such an effect from the deformation induced warpage.

The goal of this study is to broaden the range of suitability of the applications of shadow moiré as a surface profiling technique. To reach that objective a new shadow moiré system is to be developed that will incorporate some new algorithms and techniques to overcome the existing limitations. To that end, the scopes of the research are defined as:

- Propose and implement a new phase unwrapping algorithm that will impose no restrictions on the size of the phase data array.
- Incorporate suitable digital image processing techniques that will facilitate the measurement in non-rectangular or irregular shaped surfaces and hollow areas.
- Find a practicable and convenient scheme that will result in increased accuracy in the system sensitivity calibration.

- Normalize the surface warpage data in reference to a plane common to different measurements in a single test to eliminate the effect of possible rigid body rotation or translation during the test.
- Design special experiments for the verifications of effectiveness of the implemented algorithms and schemes.

CHAPTER 2 SHADOW MOIRÉ BASICS AND COMPUTER AUTOMATION

Conventional in-plane moiré methods rely on a pair of similar gratings that interfere to produce a fringe pattern. The shadow moiré method employs a master (reference) grating made on a flat glass plate and placed over the specimen surface in a close distance. There is no second piece of grating needed since as the illuminating light casts the shadow of the reference grating onto the specimen, a virtual grating is formed on the surface. The surface to be measured is usually white-painted to become diffusively reflective, which improves the contrast of the virtual grating and in turn, the visibility of moiré fringes. A collimated light that illuminates a flat surface through a parallel reference grating will normally produce no moiré effect. For a warped surface, however, the virtual grating will be distorted in accordance with the surface's profile. A moiré fringe pattern is resulted due to the slight difference in pitch and line orientation between the two gratings, as typically shown in Fig.2.1.

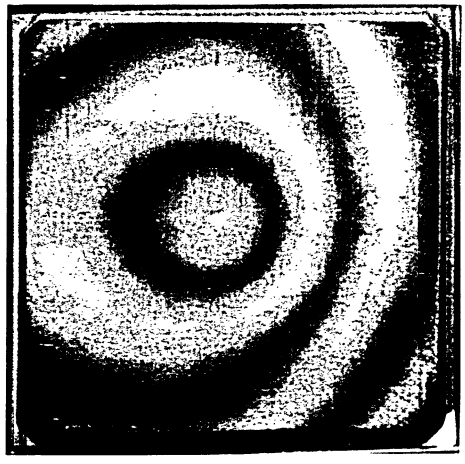

Fig.2.1 Shadow Moiré Fringe pattern induced by Interference.

2.1 Shadow moiré fringe formation and interpretation

A schematic of the shadow moiré setup [6-10,12,16,20] is given in Fig.2.2 for the analysis of fringe formation. The geometric optics is applied in the following fringe analysis, in which a light beam originated from an illumination source is traced. The light propagates through the transparent spaces in the glass grating and reaches point A, B, C, D and E on the specimen surface. Light that strikes A, C, and E is reflected back to the observer via clear spaces in the grating. Therefore, the bright moiré fringes are generated and located near A, C and E. Light that reaches points B and D is blocked by the opaque bars of the grating. As a result, the dark fringes are viewed near B and D.

If the fringe order at point A is set to be $N = 0$, then the orders at C and E are 1, and 2, respectively. A trigonometric analysis in the enlarged region around point E, provides the geometric relationship as below:

$$W(x, y) = N(x, y)p/(\tan\alpha + \tan\beta) \tag{2.1}$$

where $W(x, y)$ represents the distance from a point (x, y) on the surface to the glass grating, α and β are the illumination angle and observation angle, respectively, $N(x,y)$ is the fringe order at the point, and p is the pitch of the grating.

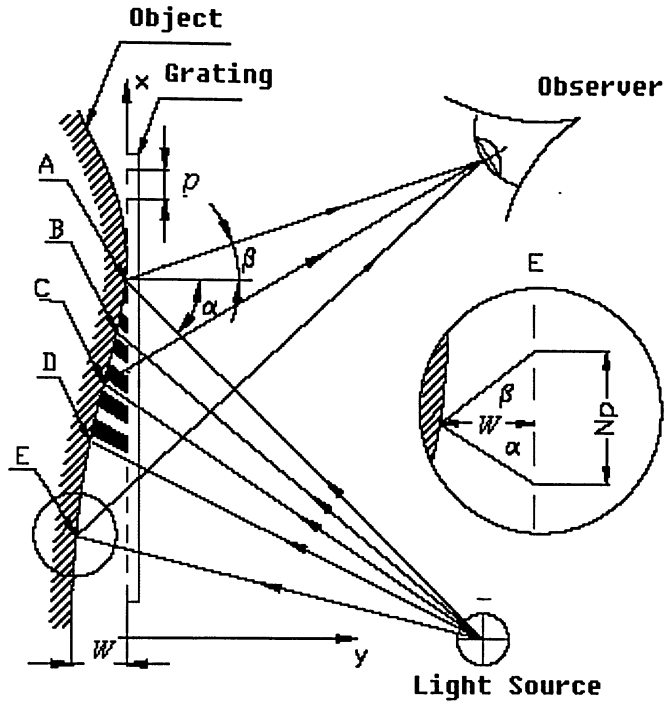

Fig.2.2 Geometry of shadow moiré. [16]

For the sake of convenience, Eq.2.1 is often expressed as

$$W(x,y) = N(x,y)\,w \tag{2.2}$$

where $w = p/(\tan\alpha + \tan\beta)$ is a constant defined as the *system sensitivity*, and the value of w depends on the optical setup used. For a given shadow moiré setup used in an application, w is not usually obtained by calculation. Instead w is more often determined via system calibration which will be discussed in detail in Chapter 3.

Warpage W at a surface point is calculated by knowing the system sensitivity w and the order of fringe N at a point. N is not necessarily an integer, but to determine the fractional fringe order at a point via the light intensity at the point has proven to be challenging.

Instead, a phase shifting technique is applied to determine the phase term of the fringe pattern at the point. Knowing the phase angle ϕ at the point, the fractional order N at the point can be more precisely obtained via Eq.1.12, which is rewritten as below

$$N(x, y) = \frac{\phi(x, y)}{2\pi} \qquad \text{(1.12) or (2.3)}$$

The phase-shifting technique will be discussed in detail in Section 2.4. The setup as shown in Fig.2.3 employs a point light source, which renders both the illumination angle α and the observation angle β to vary from point to point over the measured area. This suggests that the system sensitivity could vary depending on the location of the point. An arrangement like such will make the fringe interpretation complicated. Preferably, $W(x,y)$ would rather be proportional to the fringe order $N(x,y)$. A possible solution to avoid such complication is to arrange the system setup in a way that the light source and the camera are positioned at the same height L from the plane of the grating. A further analysis [1,16] has come to the conclusion that, with such an arrangement, the term $(\tan\alpha + \tan\beta)$ is determined by

$$\tan\alpha + \tan\beta = D / L \qquad (2.4)$$

where D is the distance between light source and camera. Eq.2.1 is thus reduced to

$$W(x, y) = \frac{N(x, y) pL}{D} \qquad (2.5)$$

A constant system sensitivity $w = pL/D$ is therefore obtained. If the distances D and L are equal, Equation 2.5 is further simplified to $W = Np$.

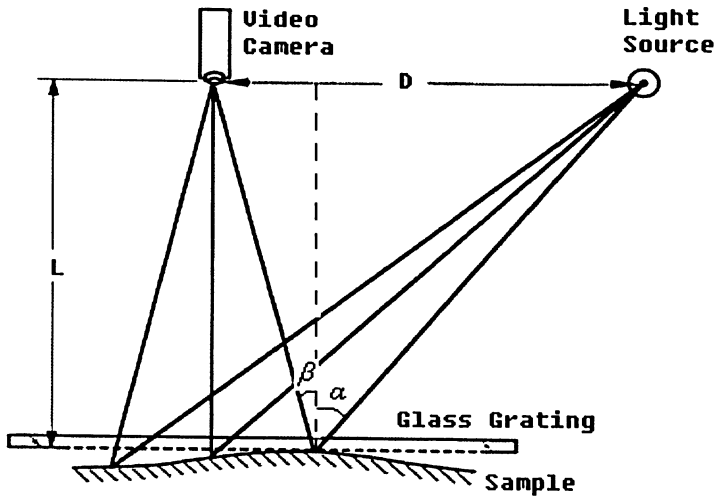

Fig.2.3 Shadow moiré with configuration of normal viewing. [16]

The set-up configuration shown in Fig.2.3 represents a most popular arrangement in which the camera is positioned perpendicular to the plane of the specimen's supporting fixture. The governing equation for such a setup becomes

$$W(x,y) = N(x,y)p / \tan\alpha \qquad (2.6)$$

In addition to the constant fringe sensitivity, the normal viewing setup has the advantage of reduced image distortion due to the perspective effect that happens when the specimen is viewed at an oblique direction. In a test, the reference grating should be placed at a very close range over the specimen. Moiré pattern becomes clearly visible only when the grating and the specimen are kept very close to each other. Otherwise, the fringes will suffer a loss of contrast due to the effect of diffraction. The specimen surface is usually spray-painted to obtain a uniform diffusive reflectivity. The light is directed at an angle α, illuminating, through the grating, the surface of the specimen. The CCD camera with a zoom lens is vertically positioned. The grating mounting fixture is designed to support the

grating with high stability. The entire experimental setup is usually placed on a vibration-free table.

2.2 History of shadow moiré and computer fringe processing

In the early years of the method's development, the fringe analysis relied on manual operation. Though the surface's topography is directly visualized by the shadow moiré pattern because the fringes can be viewed as the contour lines mapping the surface topographic features. A complete fringe analysis includes locating the centerlines of the moiré fringes, counting the fringe orders and determining the signs of fringe orders (i.e., the warp directions at these locations). Half-fringe orders are assigned to those locations of the maximum or minimum brightness, where the centerlines of dark or bright fringes are identified with acceptable precision. The determination of the signs of fringe orders largely depends on the operator's experience and the prior knowledge of the behavior of similar samples. Due to these reasons, the conventional fringe analysis proved to be time-consuming and many times, ineffective and subjective.

The introduction of the digital imaging and computer-aided image processing techniques to the shadow moiré initially focused on processing small portions of fringes. Some degree of automation was achieved by adopting numerical algorithms for finding and thinning the centrelines of the fringes, assigning fringe orders and plotting the measured topographic data in the form of contour maps. With the advance of digital imaging techniques and digital image processing algorithms, Creath [5] in 1988 proposed a phase shifting technique for the automation of fringe analysis. Since then, the research for implementing phase shifting to shadow moiré fringe analysis has continued to progress. Shadow moiré

has now been accepted into many areas as a major technique for realizing full-field out-of-plane displacement measurement. For microelectronics industries, the initial adoption of automated shadow moiré happened in the late 1990s when the technique was first employed for measuring warpage of PCB (printed circuit board) subject to mechanical and thermal loading. Due to the small range of deformation, high measurement sensitivity is required in the area.

Unlike the early computerized fringe analysis, the phase shifting technique utilizes the full-field information of entire fringe pattern. The new technique is featured by employing a set of several fringe patterns, each being recorded under the same conditions except with a different amount of phase-shift. Though a recorded fringe pattern carries the information of the light intensity distribution only, the incorporation of a phase-shifting technique into the fringe processing enables the determination of the phase distributions in the patterns. The introduction of the technique results in a dramatic improvement in the shadow moiré's measurement resolution since by knowing the phase angle distribution, any fractional fringe orders can be determined with ease. Studies [4,11,24] shows that, in practical applications, a resolution of 0.01 fringe order can be reasonably expected. A detailed discussion on the phase-shifting technique is presented in the section to follow.

2.3 Phase-shifting techniques implemented to shadow moiré

When the reference grating is vertically moved toward or away from the surface being measured, the moiré fringes will shift accordingly along the fringe order descending or ascending direction. As can be understood from the schematic in Fig.2.4, the glass grating is initially located at position 1, and the dark fringes can be observed due to the

superposition of glass grating lines and shadow ones. Once the grating is moved to position 2, light fringes are observed instead, because at the position the light passes through clear space on the glass grating and reflects back to the camera. As the grating is translated to location 3 where the distance of the grating translation turns to be *w*, the dark fringes will be observed again and the appearance of the moiré pattern will be identical as the original un-shifted one. Thus, the fringes viewed from the camera are shifted by one integer order.

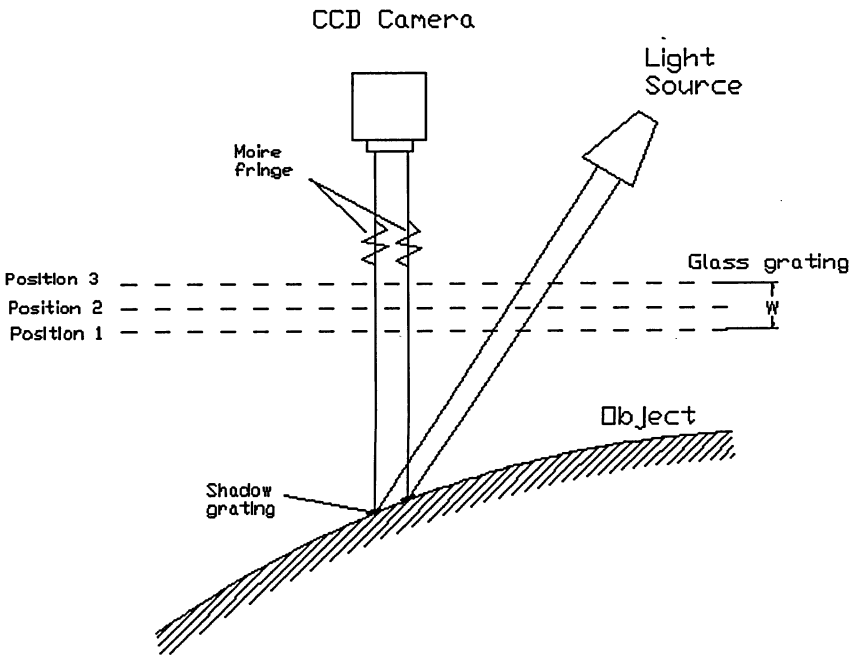

Fig.2.4 Fringe movement related to grating translation.

The determination of phase distribution by a set of phase-shifted fringe patterns to automate the fringe analysis is based on an assumed harmonic representation of the intensity variation of a moiré fringe pattern. Under that assumption, the intensity distribution of a fringe pattern can be mathematically expressed as

$$I(x,y)=A(x,y)+B(x,y)\cos[\phi(x,y)] \quad (2.7)$$

where $A(x,y)$ is the pattern's background intensity, $B(x,y)$ is the fringe amplitude and $\phi(x,y)$ is the angular phase. Three unknown terms are noted in the equation, namely A, B and ϕ. The analysis below intends to show that the unknowns are solvable if a minimum of three phase-shifted fringe patterns is made available. These patterns must be recorded under identical conditions but allowing the difference of a constant phase term. Let the set of three patterns consisting of an original pattern and two with constant amount of phase shift, $-\delta$ and $+\delta$, respectively. The fringe patterns are then represented by the following intensity equations:

$$I_1(x,y)=A(x,y)+B(x,y)\cos[\phi(x,y) - \delta]$$

$$I_2(x,y)=A(x,y)+B(x,y)\cos[\phi(x,y)]$$

$$I_3(x,y)=A(x,y)+B(x,y)\cos[\phi(x,y) + \delta] \quad (2.8)$$

In the equations δ is a known constant and the light intensities I_1, I_2 and I_3 at discrete pixel locations (x, y) are also known from the corresponding pixel readings obtainable from the digital fringe patterns. A, B, and ϕ at (x, y) are thus readily solvable with the above simultaneous equations. In particular, ϕ at (x, y) can be determined by Eq.2.9.

$$\phi(x,y) = \arctan\left[\frac{1-\cos\delta}{\sin\delta}\cdot\frac{I_1(x,y)-I_3(x,y)}{2I_2(x,y)-I_1(x,y)-I_3(x,y)}\right] \quad (2.9)$$

Specially, if δ is taken to be $2\pi/3$, Eq.2.9 becomes

$$\phi(x,y) = \arctan\left[\sqrt{3}\cdot\frac{I_1(x,y)-I_3(x,y)}{2I_2(x,y)-I_1(x,y)-I_3(x,y)}\right] \quad (2.10)$$

Equation 2.10 is commonly known as the *phase equation* for the three-step phase shifting

algorithm. Theoretically, the more fringe patterns are involved, the more accurate phase calculation will be reached [11,24,38]. Yet for time dependent applications, since the speed of image recording matters, the three-step shifting may be more advantageous. The four-step phase shifting on the other hand may be the most commonly applied algorithm due to its simple mathematics for the phase calculation. If an equal shift of $\pi/2$ is applied for each step, the four consecutively recorded fringe patterns are expressed as

$$I_1(x,y)=A(x,y)+B(x,y)\cos[\phi(x,y)]$$

$$I_2(x,y)=A(x,y)+B(x,y)\cos[\phi(x,y)+\frac{\pi}{2}]$$

$$I_3(x,y)=A(x,y)+B(x,y)\cos[\phi(x,y)+\pi]$$

$$I_4(x,y)=A(x,y)+B(x,y)\cos[\phi(x,y)+\frac{3\pi}{2}] \qquad (2.11)$$

ϕ is determined by a simple equation given as follows:

$$\phi(x,y) = \arctan[(I_4-I_2)/(I_1-I_3)] \qquad (2.12)$$

It is noted that the pixel readings inevitably contain errors of various sources. A study [37] claims that Equation 2.9 has a higher chance than Eq.2.7 to become "ill-conditioned" in terms of obtaining a near-zero denominator, whereas a five-step phase shifting with symmetric phase change, as proposed, may reduce such uncertainties in the phase solution. The five phase-shifted images are expressed as

$$I_1(x,y)=A(x,y)+B(x,y)\cos[\phi(x,y) - 2\delta]$$

$$I_2(x,y)=A(x,y)+B(x,y)\cos[\phi(x,y) - \delta]$$

$$I_3(x,y)=A(x,y)+B(x,y)\cos[\phi(x,y)]$$

$$I_4(x,y)=A(x,y)+B(x,y)\cos[\phi(x,y) + \delta]$$

$$I_5(x,y)=A(x,y)+B(x,y)\cos[\phi(x,y)+2\delta] \tag{2.13}$$

The equation yields the phase ϕ as

$$\phi(x,y)=\arctan\left[\frac{1-\cos\delta}{\sin\delta}\cdot\frac{I_2(x,y)-I_4(x,y)}{2I_3(x,y)-I_1(x,y)-I_5(x,y)}\right] \tag{2.14}$$

If δ is taken to be $\pi/2$, Eq.2.14 becomes

$$\phi(x,y)=\arctan\left[\frac{I_2(x,y)-I_4(x,y)}{2I_3(x,y)-I_1(x,y)-I_5(x,y)}\right] \tag{2.15}$$

In the current study, both three-step and four-step algorithms are studied and implemented in the shadow moiré processing. Typical results shown in Fig.2.5 are obtained from applying a three-step phase shifting algorithm to a piece of optical lens. The two-dimensional contour map plotted in Fig. 2.5 represents the distances from the surface to a reference plane. The three-dimensional surface plot gives a quick glance of the surface profile. The example shows a dramatic measurement resolution improvement when the phase-shifting is implemented. With the intensity based scheme that limits the resolution to half-fringe orders, the application of a phase-shifting technique theoretically comes up with assigning to each pixel location one of 256 possible grey values. Therefore, the new method has a resolution of 1/256 fringe order or more conservatively, 0.01 fringe order [11,24,37].

In addition to improved measurement resolution, phase shifting has another advantage of automatically determining the direction of the warpage based on the directions of fringe shifting. Owing to the whole-field nature, the phase term at every pixel location in the fringe pattern is available. Comparing the phase between adjacent pixels will indicate the phase gradient or the trend of topography in the neighbourhood.

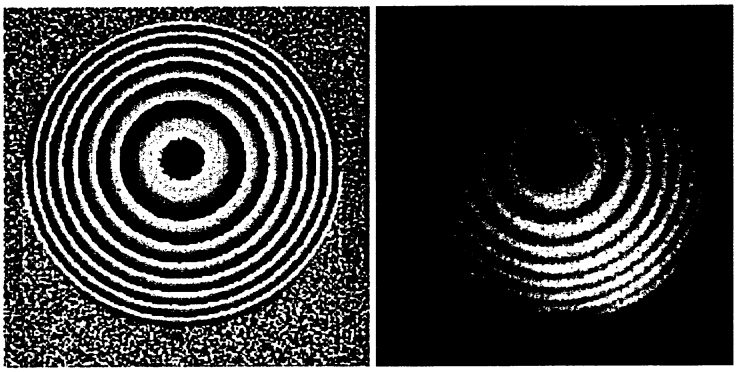

(a) Wrapped phase diagram (b) Unshifted fringe pattern

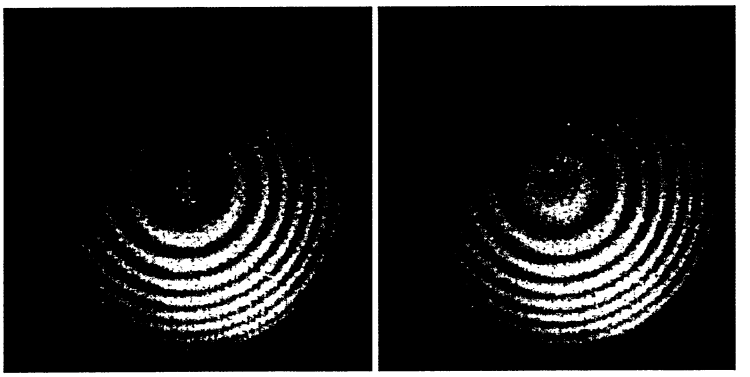

(c) $2\pi/3$ phase shifted fringe pattern

(d) $4\pi/3$ phase shifted fringe pattern

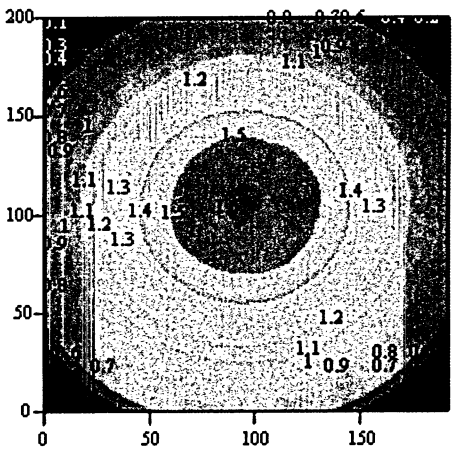

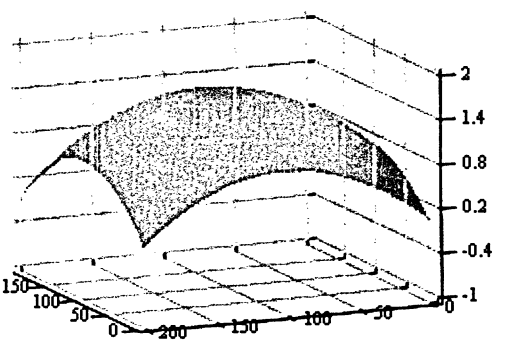

(e) 2-D presentation of unwrapped surface plot

(f) 3-D presentation of unwrapped surface plot

Fig.2.5 Fringe patterns obtained in phase shifting method and the result contours.

2.4 Phase unwrapping

Due to the nature of the arctangent as an inverse trigonometric function, only the principal value of $\phi(x, y)$, wrapped in the range of $(-\pi, \pi)$, is directly determined. The so-obtained phase angle must be unwrapped to add the multiples of 2π, if the actual value goes beyond the $(-\pi, \pi)$ range. A proper unwrapping procedure therefore must be implemented to recover the actual phase map. The general relationship between a wrapped phase and its unwrapped counterpart is expressed as follows:

$$\Phi(x,y) = \phi(x,y) + 2\pi k(x,y) \qquad (2.16)$$

where $\Phi(x,y)$ is the unwrapped phase, $\phi(x,y)$ is the wrapped phase and $k(x,y)$ is an integer number. Unwrapping is thus a process of finding the correct number k in Eq.2.16 for each phase measurement, and adding or subtracting $2\pi k$ at each discontinuity encountered in the phase data. In general, across a two-dimensional image domain, the wrapped phase diagram can show places of discontinuity when the warpage variation is greater than one fringe sensitivity w. The discontinuities occur whenever ϕ changes by 2π. This process is repeated for each pixel across the two-dimensional image domain until a continuous phase map is obtained. The unwrapped phase array is then multiplied by $w/2\pi$ to give the displacement data at each point.

Fig.2.6 shows an example of one-dimensional phase variations before and after unwrapping, in which the wrapped phase ϕ is plotted by dashed lines. The unwrapped phase Φ shown by solid line is obtained by adding an appropriate multiple of 2π radians to ϕ. It is seen that the true phase is linearly distributed, given that the wrapped phase is the

sawtooth function (shown by dashed lines).

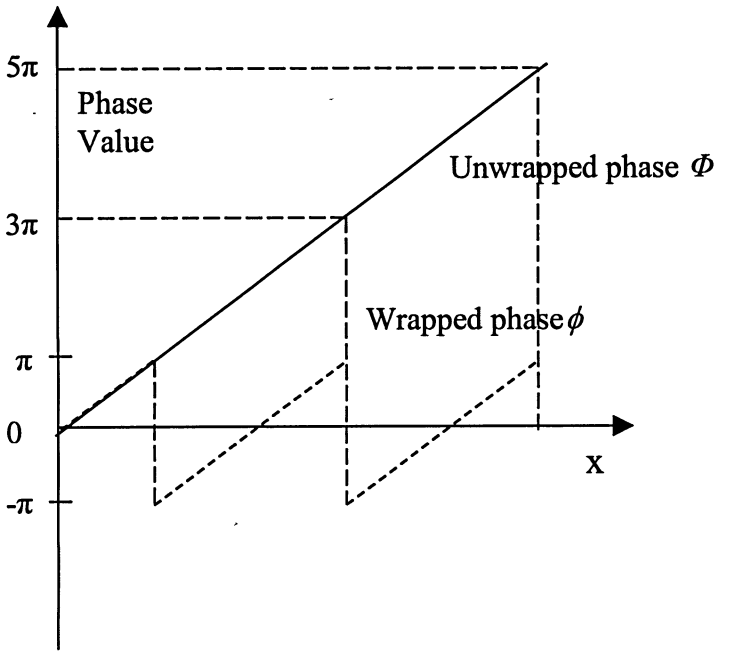

Fig.2.6 Plot of true phase and wrapped phase.

With an ideal noise-free wrapped phase image, the phase unwrapping is likely a simple and straightforward process that follows the above equation to recover the actual phase. However, for surfaces with complex geometry or noise-corrupted images, the process could be very difficult.

Common approaches for phase unwrapping in the presence of these effects are categorized into two groups, namely the path-following methods and least-square methods. The path-following algorithms detect the location of errors or abrupt phase steps in an image. Based on the information, the approach isolates the phase inconsistencies and chooses an unwrapping path that does not cross the errors, thereby preventing the phase errors from

propagating. This approach has low computational cost, but is difficult in choosing correct paths when the phase discontinuities are very densely distributed. Least-square unwrapping belongs to global algorithms in terms of minimization of global phase inconsistencies. Compared to path-following approaches, least-square algorithms are robust but computationally intensive. The following section gives an in-depth discussion on the latter approaches.

2.4.1 Least-square phase unwrapping algorithms

Least squares phase unwrapping, established by Ghiglia and Romero [58], is one of the most robust techniques to solve the two-dimensional phase unwrapping problem. Its unwrapped phase is the solution that minimizes the differences between the discrete partial derivatives of wrapped phase data and the discrete partial derivatives of the unwrapped solution.

Given the wrapped phase $\phi_{i,j}$ on an M x N rectangular array ($0 \le i \le M-1$, $0 \le j \le N-1$), the partial derivatives of the wrapped phase are described by

$$\Delta_{i,j}^{x} = W\{\phi_{i+1,j} - \phi_{i,j}\}, \quad \Delta_{i,j}^{y} = W\{\phi_{1,j+1} - \phi_{i,j}\} \tag{2.17}$$

where W is a wrapping operator that holds the phase in the interval [-π, π].

The differences between the discrete partial derivatives of wrapped phase data and the discrete partial derivatives of the unwrapped solution are given by

$$\varepsilon^2 = \sum_{i=0}^{M-2}\sum_{J=0}^{N-1}(\Phi_{i+1,j} - \Phi_{i,j} - \Delta_{i,j}^{x})^2 + \sum_{i=0}^{M-1}\sum_{j=0}^{N-2}(\Phi_{i,j+1} - \Phi_{i,j} - \Delta_{i,j}^{y})^2 \tag{2.18}$$

where $\Phi_{i,j}$ is unwrapped phase on an M x N array.

Differentiating the Equation with respect to $\Phi_{i,j}$ and setting the result equal to zero yields the following discrete Poisson function:

$$\Phi_{i,j} = \frac{(\Phi_{i+1,j} + \Phi_{i-1,j} + \Phi_{i,j+1} + \Phi_{i,j-1}) - \rho_{i,j}}{4} \tag{2.19}$$

where

$$\rho_{i,j} = (\Delta^x_{i,j} - \Delta^x_{i-1,j}) + (\Delta^y_{i,j} - \Delta^y_{i,j-1})$$

The classical method for solving the discretized Poisson equation is called Gauss-Seidel relaxation. It solves the equation by initializing the solution array $\Phi_{i,j}$ to zero and then updating $\Phi_{i,j}$ in an iterative way until convergence is reached.

2.4.2 Multi-Grid phase unwrapping algorithm

Gauss-Seidel relaxation extracts the high-frequency components of the surface (i.e., the surface details) very quickly, but the low-frequency components (i.e., the global structure of surface) extremely slow. Due to that, a multi-grid method was introduced. The idea behind the multigrid method is to convert the low-frequency components to high-frequency ones, thus to speed the convergence. This is implemented by transferring the problem from finer grid to coarser grid, as illustrated in Fig.2.7. In this figure, each grid has one-half resolution of its predecessor. The finer grid and coarser grid are denoted $f_{i,j}$ and $c_{i,j}$, respectively.

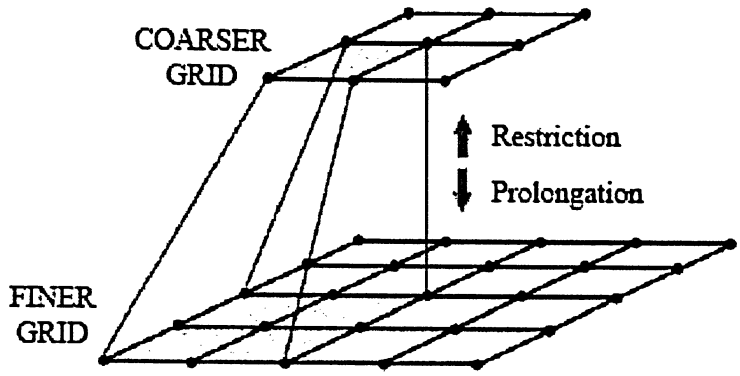

Fig.2.7 Multigrid algorithm using Restriction and Prolongation operations. [56]

The process has two operators, one being called restriction operator for transferring the problem to a coarser grid. The other is prolongation operator for transferring the solution to a finer grid. A full weighting restriction operator [56] is used in this study and is defined by

$$c_{i,j} = \frac{1}{16}(f_{2i-1,2j-1} + f_{2i+1,2j-1} + f_{2i-1,2j+1} + f_{2i+1,2j+1}) \qquad (2.20)$$
$$+\frac{1}{8}(f_{2i,2j-1} + f_{2i,2j+1} + f_{2i-1,2j} + f_{2i+1,2j})$$

This full weighting operator is actually a smoothing process with the following non-linear filter template.

$$\begin{bmatrix} 1/16 & 1/8 & 1/16 \\ 1/8 & 1/4 & 1/8 \\ 1/16 & 1/8 & 1/16 \end{bmatrix}$$

The bilinear interpolation is used for prolongation operator and is given by

$$
\begin{aligned}
f_{2i,2j} &= c_{i,j}, \\
f_{2i+1,2j} &= \frac{c_{i,j} + c_{i+1,j}}{2}, \\
f_{2i,2j+1} &= \frac{c_{i,j} + c_{i,j+1}}{2}, \\
f_{2i+1,2j+1} &= \frac{c_{i,j} + c_{i+1,j} + c_{i,j+1} + c_{i+1,j+1}}{4}.
\end{aligned}
\tag{2.21}
$$

The operation of multigrid algorithm is simply described as follows:

1) Perform Gauss-Seidel relaxation on finest grid and restrict the intermediate solution to the next coarser grids.

2) Repeat this process until it reaches the coarsest grid, whose size is defined here as 3x3.

3) Transfer the intermediate solutions back to finest grid using prolongation operator and perform relaxation on each grid.

4) Transfer back and forth between finest and coarsest grids until convergence reached.

2.4.3 Comparison of phase unwrapping methods

Poisson discretized function can also be solved by using Fast Fourier Transform (FFT) and Discrete Cosine Transform (DCT) algorithms. FFT and DCT are less computationally expensive and have less computer memory requirements than the multi-grid algorithm. However, FFT and DCT methods have the restrictions on the size of the phase array, which must be powers of two, and can solve less classes of unwrapping problems in terms of successes and failures on the phase unwrapping examples [56,60,61,62]. Compared with the FFT and DCT least-square unwrapping techniques that are commonly applied to the phase shifted shadow moiré methods, multigrid algorithm is advantageous.

2.5 Computer-automated shadow moiré system realization

The system as schematically described in Fig.2.8 consists of the sub-systems with different functionalities, which are described as follows:

- **Digital image recording**

A CCD camera of maximum frame rate of 30 frames per second (Javelin Ultrachip Hi Res) equipped with a NAVITAR 6000II lens combination consisting of a 0.5x adapter, 6.5x prime lens and 0.25x lens attachment, is used to record the fringe patterns. A Matrox Meteor II image grabber is installed into a desk-top computer and used for image digitization. The digital images are recorded in format of 640 (horizontal) x 480 (vertical) pixels. The 8-bit binary signal gives pixel reading in 256 grey levels for light intensity variation, ranging from 0 (black) to 255 (white).

- **Light illumination**

An incandescent light source with adjustable light intensity is employed. The light is transmitted through an optic fiber bundle. The angle of illumination is realized by adjusting the posture of the head of fiber bundle. The light source is positioned at the same height as the camera for constant fringe sensitivity.

- **Glass grating**

A high-temperature resistant glass grating with low CTE (Coefficient of Thermal Expansion) is used in applications involving elevated temperature. The size of the glass grating should be sufficient to cover the area of interest in a sample surface. The glass

grating of the line density of 10 or 20 lpmm (lines/mm) is normally used. The higher the grating density, the higher the measurement sensitivity the system can reach.

- **Micro-motion stage**

The glass grating is mounted in a micro-motion stage that provides three-dimensional translation and three directions of tilt for adjusting the position of the grating. Fig.2.9 shows the drawing of a 3-D, 6-axis micro-stage that is normally placed outside the thermal chamber, along with a grating holder. The stage enables the fringe pattern phase shifting by lifting or lowering the glass grating over the sample.

- **Thermal chamber**

An Instron 31900 programmable thermal chamber with a temperature variation range between -70 and 250°C is applied to the system. The maximum ramp-up rate the chamber can reach is 8 °C / minute. The cooling progress is realized using pressurized liquid carbon dioxide (CO_2)

- **Optical vibration-isolation table**

A Newport table is used to provide the measurement system with a vibration-free and superior-flat platform.

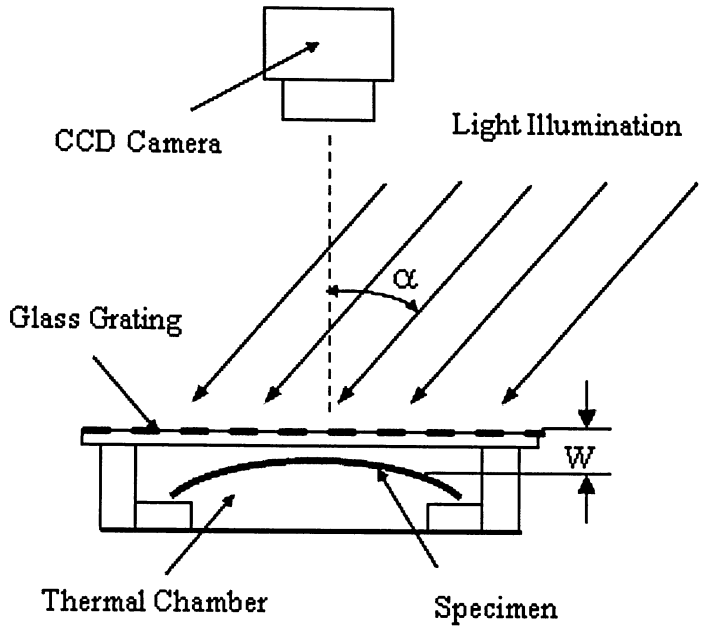

Fig.2.8 Experimental setup of shadow moiré method.

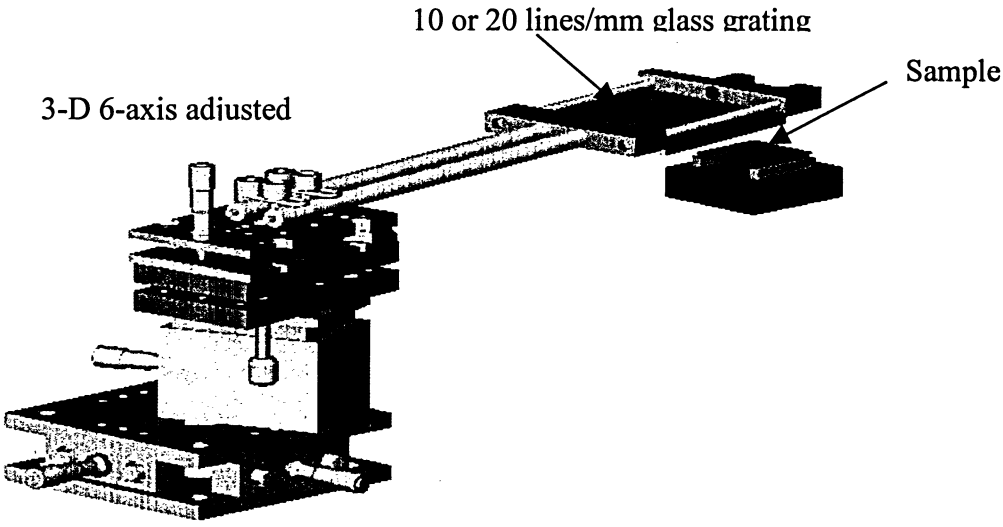

Fig.2.9 Three-dimensional, 6-axis micro-motion stage with glass grating.

CHAPTER 3 IMAGE PROCESSING TECHNIQUES APPLIED TO SHAODW MOIRE

3.1 Noise reduction from phase diagrams

3.1.1 Noise in digital images

Digital images are often corrupted by random noises appearing as speckles in the images. The noise can be generated during image recording, processing and transmission. The common modes of digital image noises can be categorized into the independent noise and the dependent noise. The independent noise is usually additive noise [53,54]. A pixel reading in a noisy image is the sum of original pixel value and a random noise, and a noise corrupted image f is related to the noise v by

$$f(x,y) = g(x,y) + v(x,y) \tag{3. 1}$$

where the noise v and the noise-free image g are both independent variables. Gaussian noise [54,55] that exists in signals of many electronic devices falls in this category. The noise distribution in the image domain can be described by a Gaussian function as follows:

$$p(x) = \frac{1}{\sigma\sqrt{2\pi}} e^{\frac{-(x-\mu)^2}{2\sigma^2}} \tag{3.2}$$

where μ is the mean and σ the standard deviation of the random variable.

According to the Gaussian noise theory, an amount of the noise will scatter to all parts of an image so that each original pixel reading will be affected though usually by a small

amount. Impulsive noise is another additive form of noise. For images affected by such noise mode, the brightness of an impulsive noisy pixel differs significantly from other pixels in its neighbourhood. Salt-and-pepper noise is a typical kind of saturated impulsive noise that appears as dark and white dots in the image display. The grey level of a salt-and-pepper noisy pixel has no relation to those of surrounding pixels.

Multiplicative noise is an image dependent noise mode and its magnitude $f(x, y)$ is generally expressed as

$$f(x,y) = g(x,y) + v(x,y)g(x,y) \qquad (3.3)$$

where $g(x, y)$ is the original signal, $v(x,y)$ is a factor of multiplication and $v(x,y)g(x,y)$ represents the noise. If the magnitude of the signal is much higher than the noise, Eq.3.3 can be simplified to

$$f(x,y) = v(x,y)g(x,y) \qquad (3.4)$$

As shown above, the image dependent noise has a more complicated structure. To approximately treat the noise as image independent, where possible, is preferred.

3.1.2 Noise affected phase diagram and treatment

Grey scale values of an image recorded during an application inevitably contain errors or noises that stem from internal and external sources of the measurement system. Image noise in essence is the unwanted variation of recorded light irradiance of a measured surface. The noise is mainly caused due to instability of electronics, environment and light illumination. At a given time instant, the variation may be high at certain pixel location

while low at others. The noise in the digitized image pixel readings will propagate, resulting in a noisy phase diagram. A typical example is the phase term of a background point. According to the theory and the mathematic approach proposed in section 2.3.3, the background point is assigned to zero phase angle. But in a practical case, non-zero phase may be obtained as a result of the noise corruption. Such a situation may happen to pixel locations that give $I_1 = I_3$ yet $I_2 \neq I_4$. At these locations, infinitive phase solutions are obtained from Equation 2.9. A phase diagram that contains such impulsive noise in the background area exhibits independent dark and bright spots. Such noise is typical salt-and-pepper noise and is considered a dominant source of degradation for the current phase diagram. In section 2.3, an approach is proposed to distinguish background from the measured area. Basically, the approach sets the phase solution to zero wherever a zero denominator occurs. This approach needs to be further amended as follows in order to be effective when noise exists. The scheme treats any such point as a background point, where any two of the four given intensities I_1, I_2, I_3 and I_4 are the same. Fig.3.1 (a) and (b) show a phase diagram obtained by applying the classic scheme and that by proposing new scheme. As compared to Fig.3.1 (a), following the proposed scheme a much less noisy phase diagram is generated to clearly distinguish the background from foreground. The noise can be further eliminated applying certain noise filters such as median filter, as discussed in the section to follow.

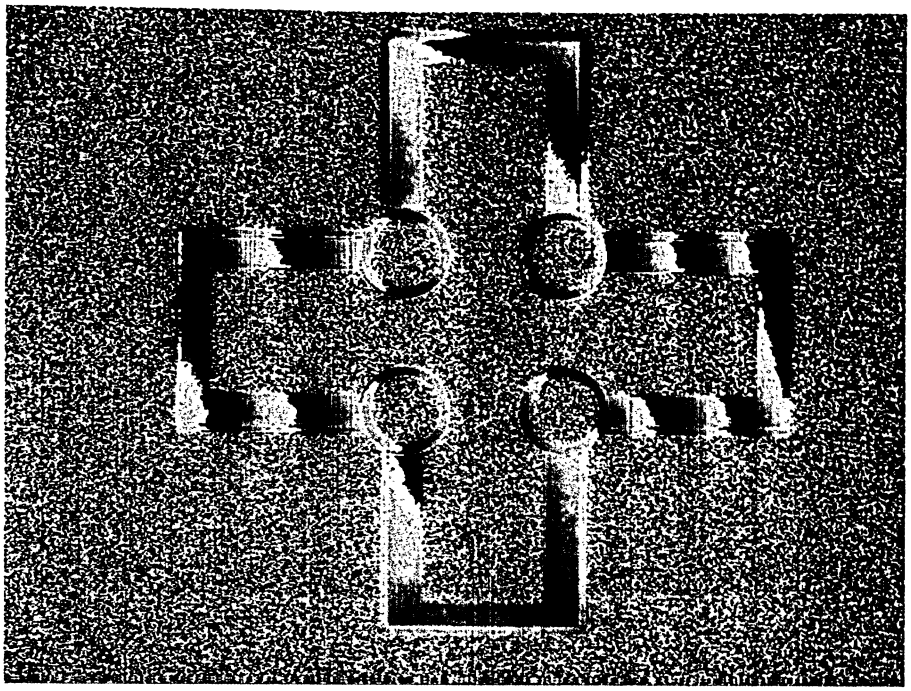

(a)

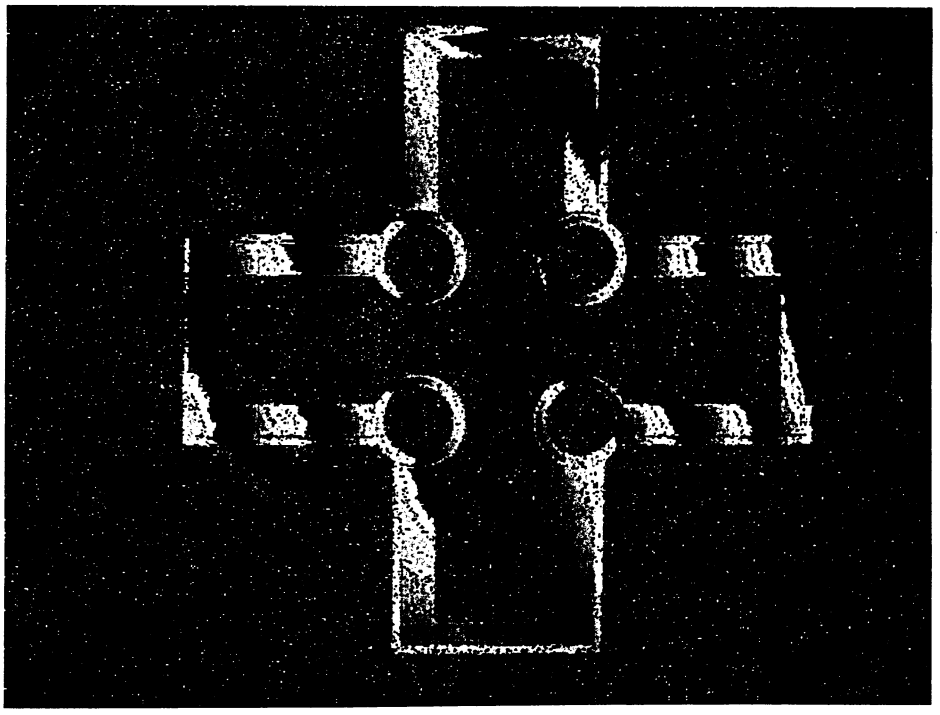

(b)

Fig.3.1 (a) Phase diagram of an antenna corrupted by noise
(b) Phase diagram with less noise after using proposed scheme
(c) Phase diagram after 5x5 Median filtering.

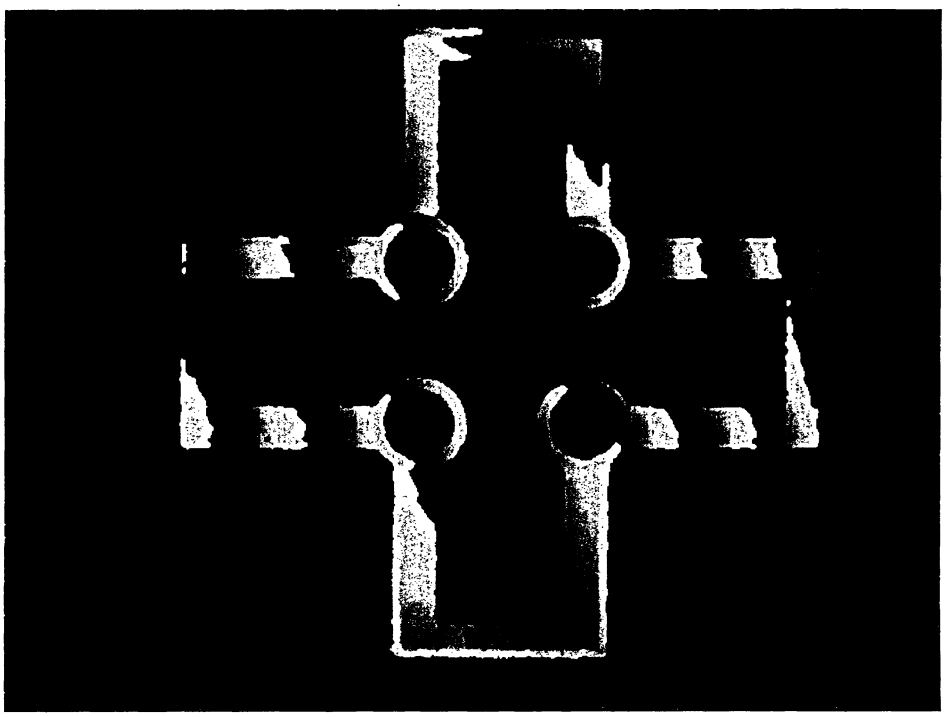

(c)

Fig.3.1 (continued).

3. 1.3 Noise reduction filters

Average Filters

Average filters are used to smooth the local variation of an image. The filters tend to blur an image by removing some details in suppressing the noise effect. The output of such smoothing process is simply the average of the gray levels of pixels contained in the region of a filter mask. The masked area is commonly a square or rectangle centred at the specified point.

Take an example as illustrated in Fig.3.2 in which the centre of a 3x3 mask moves from pixel to pixel, starting at the top-left corner of an original image and going on to cover every region in the image. As a result, every pixel reading of the image is replaced with the mean value of a corresponding filter mask. This process generates a new image with reduced sharpness and smoothed appearance. To smooth the object surface, this study implements an average filter after median filtering, which will be discussed in latter section, on the original data array in post data processing. A simple 3 x 3 pixel filter mask is defined by

$$\frac{1}{9}\begin{bmatrix} 1 & 1 & 1 \\ 1 & 1 & 1 \\ 1 & 1 & 1 \end{bmatrix}$$

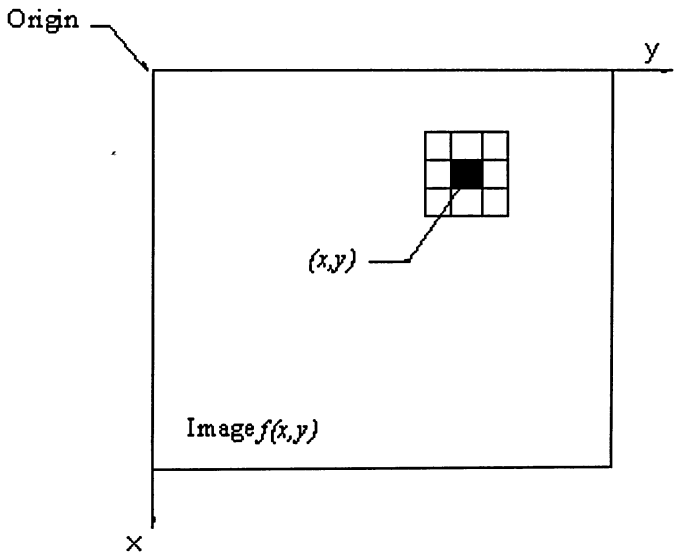

Fig.3.2 A 3x3 neighborhood around a point (x,y) in an image.

Figure 3.3 and 3.4 illustrate the typical effects of the noise reduction and edge blur when average filtering is applied. As shown, the average filtering works well with Gaussian

noise corrupted images, but even deteriorates the quality of the image while filtering salt and pepper noise.

(a) (b)

Fig.3.3 (a) Lena image with Gaussian noise [53]

(b) Image after 3x3 averaging filtering.

(a) (b)

Fig.3.4 (a) Lena image with Salt and Pepper noise [53]

(b) Image after 3x3 averaging filtering.

Orders statistics filters

Order statistics filters are nonlinear spatial filters, which are based on ranking the gray levels of pixels in the region covered by filter mask, and then replacing the value of the centre pixel with that determined by the result of a predetermined ordering scheme. The median filter is a well-known order statistics filter and similar to the averaging filter, except that the median filter uses the median value of the gray levels in the mask-covered area instead of the average.

The median value, denoted ξ, is defined such that half of the grey values in the filter neighbourhood are less than or equal to ξ and the other half are greater than or equal to ξ. Before performing median filtering on an image, it needs to sort the values of the pixels in the filter neighbourhood, determine their median, and then assign the median value to the center pixel. Unlike the average filter, median filters are popular and effective in reducing impulsive noises such as salt-and-pepper noise while preserving the edges in the image and introducing little blurring effect.

Figure 3.6 (a) and (b) show respectively the results of median filtering with a mask of size 3x3, when the images contain salt-and-pepper noise and Gaussian noise. As the pictures show, the median filter significantly reduces the salt-and pepper noise but is less effective in removing the Gaussian noise.

Fig.3.5 (a) Lena image with Salt and Pepper noise [53] (b) Image after 3x3 Median filtering.

Fig.3.6 (a) Lena image with Gaussian noise [53] (b) Image after 3x3 Median filtering.

The reason is that in the latter case the noise in the center pixel differs not much from its neighbouring pixels. Due to these reasons, the current study employs a Median filter to remove the salt-and-pepper noise in the wrapped phase diagrams as well as the impulsive noise in the unwrapped phase solutions.

3.2 Differentiate object from background by image segmentation

To automate the shadow moiré measurement, a key step is to automatically identify the boundary of the measured surface. The current study intends to enable such capability by incorporating a contour detection technique [64]. With such a technique implemented, the fringe analysis can be limited within the boundary-defined area and irregular shaped surfaces including hollowed ones can be analyzed with no need of human intervention. The study involves a few basic image-processing schemes.

3.2.1 Boundary extraction techniques

Binarizing the image

The digital images captured in this study are 8-bit monochromatic with gray levels ranging between 0 and 255. Since certain processing algorithms adopted below apply to binary images, a binarization operation is needed to convert the original 8-bit images into binary ones. The process is simply to re-assign pixel gray values to either 0 (dark) or 255 (bright) with a chosen threshold gray value.

Morphology algorithm

A morphological algorithm is introduced to extract the boundaries of an object and to differentiate it from its background. The morphological algorithm is fundamentally built

on the two transformation operations, namely, dilation and erosion, which are discussed in the following. Both transformations involve an image A and a structuring element B. Let A be the image being processed and B a set of image elements of A, both being in Z^2. The translation of B by x, denoted B_x, is defined as

$$B_x = \{c \mid c = a + x, \text{ for } a \in B\} \tag{3.5}$$

where a and c are both elements of set B. Dilation of the image A by the so-called structuring element set B, denoted $A \oplus B$, is defined by

$$A \oplus B = \{x \mid B_x \cap A \neq \Phi\} \tag{3.6}$$

Equation 3.6 is based on the shift of B by x. The dilation of A by B is the set of all displacements, x, such that B and A overlap by at least one pixel. In essence, the dilation operation allows an image to expand and thus to potentially fill in small holes and to connect discontinuities. Figure 3.7 illustrates a simple example where A is a rectangle and B is a 3x3 square template. The dashed line in the figure indicates the result of dilating the original image A with structuring element B.

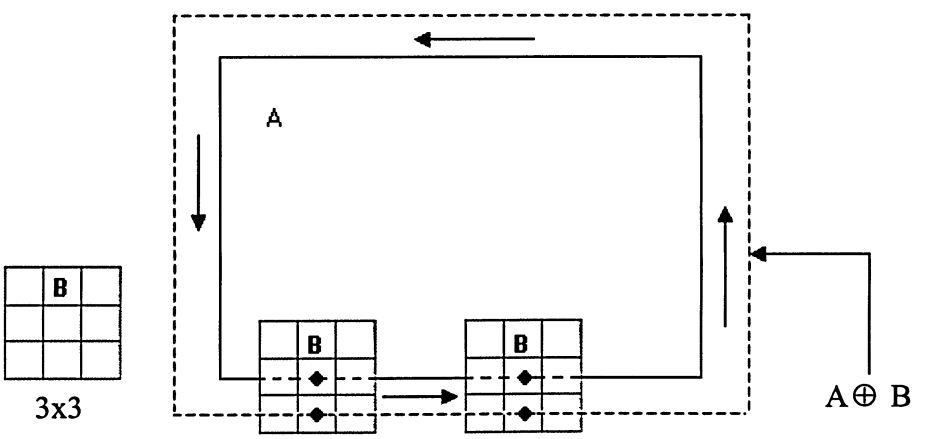

Fig.3.7 Dilation of A by structuring element B.

Erosion of an object A by a structuring element B, denoted $A \ominus B$, is given by

$$A \ominus B = \{x \mid B_x \subseteq A\} \qquad (3.7)$$

The erosion process, as explained by Fig.3.8, is opposite to the dilation. Before erosion of an original image A by element B, the boundary of A is illustrated with solid lines. The A eroded by element B is given by the internal dashed shape. Erosion shrinks an image by etching away its boundary.

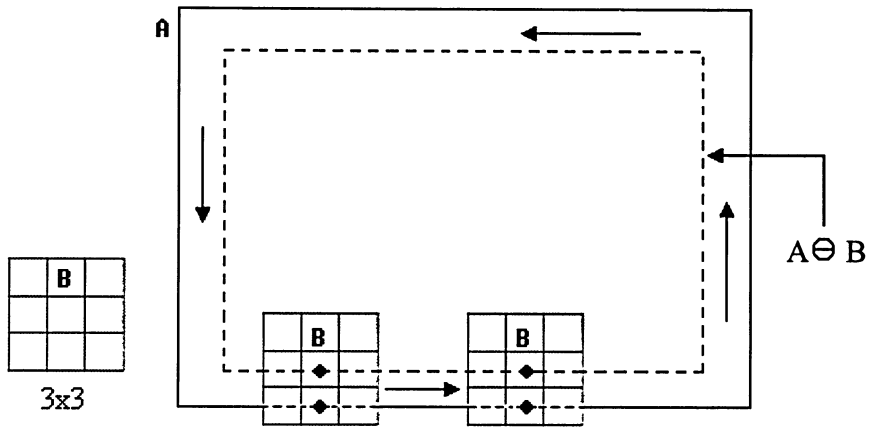

Fig.3.8 Erosion of A by structuring element B.

Boundary extraction

The operations of dilation and erosion are usually customized with a proper combination and a selection of the structuring element, which determines exactly how the image will be dilated or eroded. Boundary extraction is one of the most important morphological applications. The boundary of an image A, denoted $\beta(A)$, can be determined by first eroding A by structuring element B, and then performing the set difference between A and its erosion:

$$\beta(A) = A - A \ominus B \tag{3.8}$$

Figure 3.9 illustrates the use of equation 3.8 to extract the inner and outer boundaries of the simple binary image, in which a 3x3-structuring element is applied.

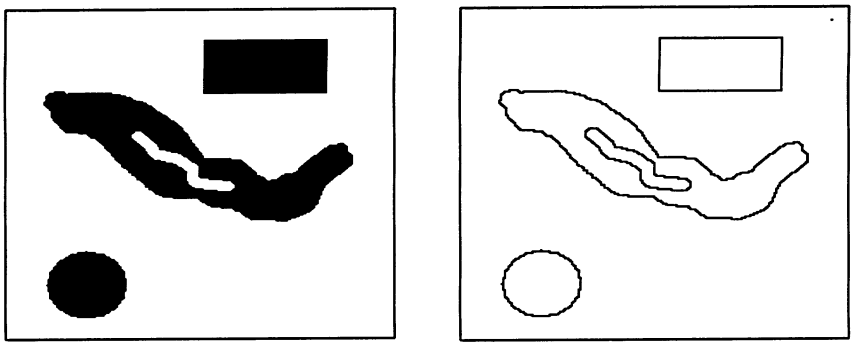

Fig. 3.9 (a) A simple binary image, (b) Boundaries extracted using Eq.3.8.

Figure 3.10 shows the moiré fringe pattern, phase diagram, inner and outer boundaries and 2-D and 3-D surface profiles of an antenna. Fig. 3.10 (e) gives 3-D warpage of the antenna with background removed applying the boundary extraction technique. In comparison, Fig. 3.10 (f) shows the warpage of the antenna along with the noisy background that is irrelevant to the analysis.

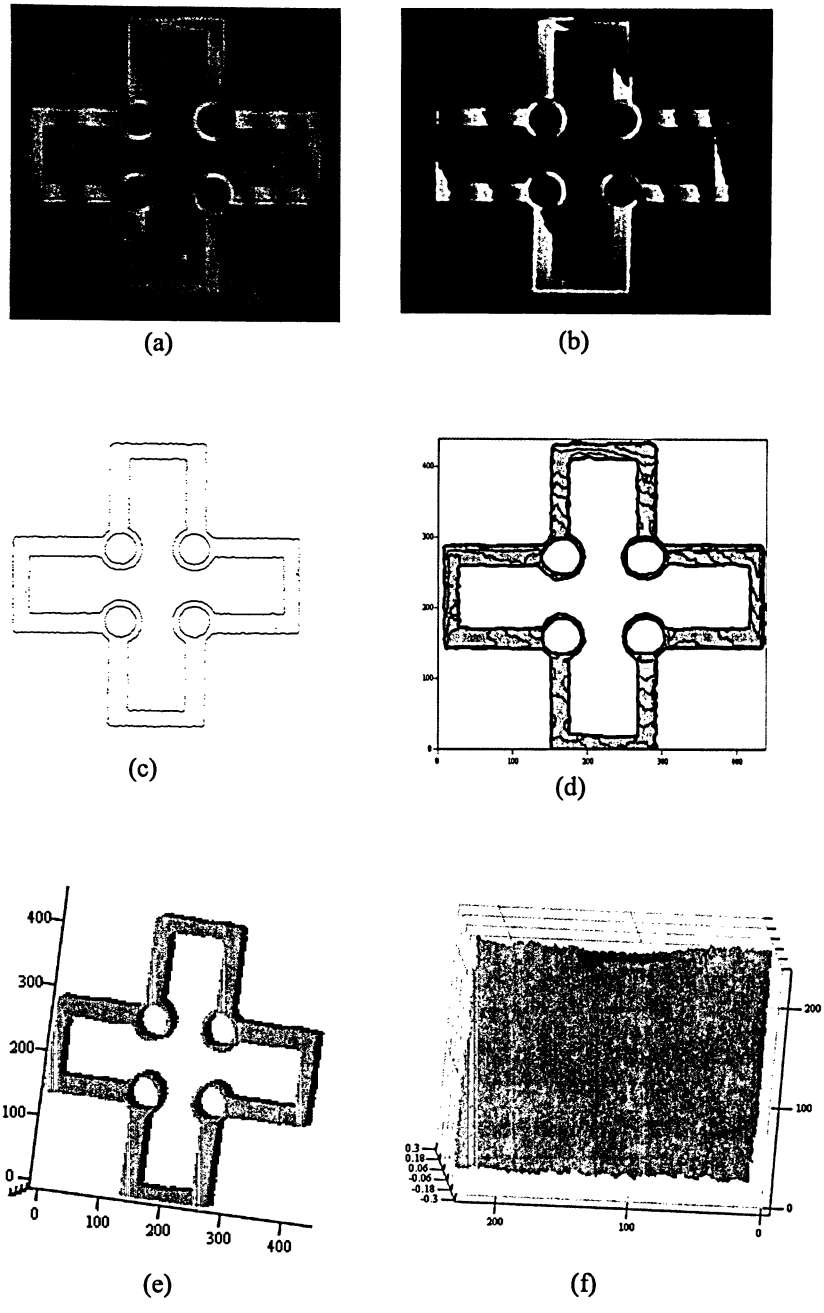

Fig.3.10 Warpage measurement for an antenna structure: (a) image with moiré fringes (b) noise-free phase diagram (c) detected inner and outer boundaries (d) 2-D surface warpage contour map (e) 3-D plot of warpage after background removed (f) 3-D surface warpage plotted with background.

3.2.2 Outer boundary tracing [54,64]

The morphological theory based boundary extraction algorithm is capable of tracking both the outer and inner boundaries. The case illustrated in Fig.3.10 shows an irregularly shaped object that has an inner hollow area. The boundary of the inner hole can be extracted along with the outer boundary of the object. Such holes or hollow areas are not always of interest in applications. If only outer boundaries are to be extracted, the Moore-neighbour tracing technique can be adopted, which is based on the concept of Moore-Neighbour of a specific pixel. The Moore-Neighbour of a pixel P is defined as a set of 8 pixels that share a vertex or edge with P. The pixels are named as 1, 2, 3, 4, 5, 6, 7 and 8, which also represent 8 directions the central pixel P travels to find the next contour pixel, as shown in Fig.3.11.

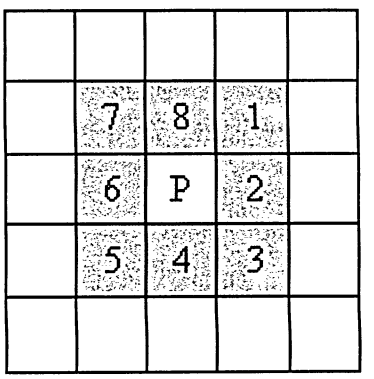

Fig.3.11 Moore Neighbour.

Given a binary pattern composed of a group of black pixels and white background pixels, as shown in Fig.3.12, the first step is to search for a start pixel by scanning the bottom row pixel-by-pixel from left to right starting from the left-bottom corner, and proceeding row-by-row until the first encounter of a black pixel **P**.

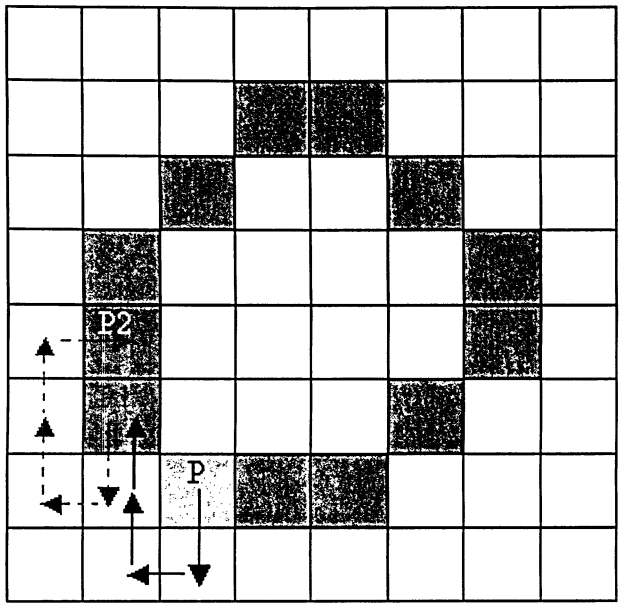

Fig.3.12 Outer boundary tracing scheme.

The algorithm, illustrated in Fig.3.12 by assuming a man traveling on the pattern to find the boundary, extracts the contour by visiting the eight positions in the Moore neighbour of the pixel **P** clock-wisely. The man starts from **P** and travels in the clockwise direction shown by the solid arrows in Fig. 3.12 until he meets the first black point **P1**. With the new starting point **P1,** the man goes back to the white point before encountering **P1** and begins the next round search as indicated by the dashed arrows until he hits the next black point **P2**. The process repeats and terminates when the first start point **P** is re-visited. All the black points he passed by will compose the contour (edge) of the pattern. Fig.3.13 (b) shows the outer contour of the pattern using the Moore-Neighbour tracing algorithm.

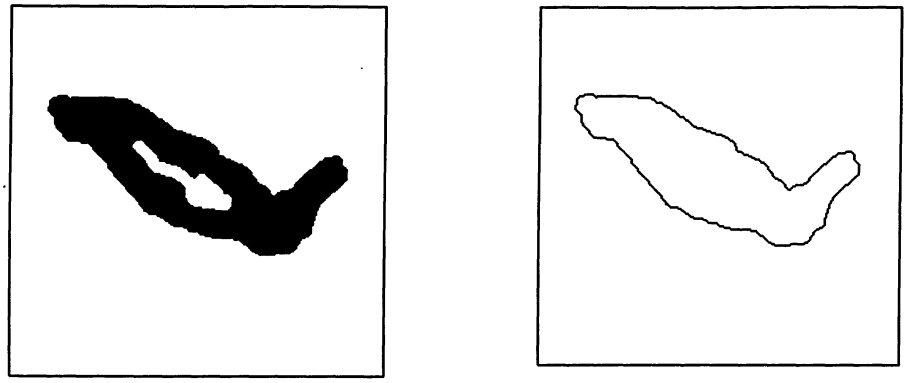

(a) (b)

Fig. 3.13 (a) A simple binary image, (b) Outer contour detected by Moore-Neighbour tracing technique.

3.2.3 Image segmentation

Once the inner and/or outer boundaries of an object are detected, the image is segmented into background and object areas. The background is eliminated so that only the object area is reserved for further analysis. Shown in Fig.3.14 is the result from experiments conducted for measuring topography for a coin. The outer boundaries of the coin were successfully detected using the Moore-Neighbour tracing technique and the analysis was performed within the identified boundaries area only. Image (f) shows a 3-D surface profile of the coin in a rectangular area. As seen from the image (b), the area outside of the coin surface is noise-distributed and usually not of interest in determining topography or warpage of the object.

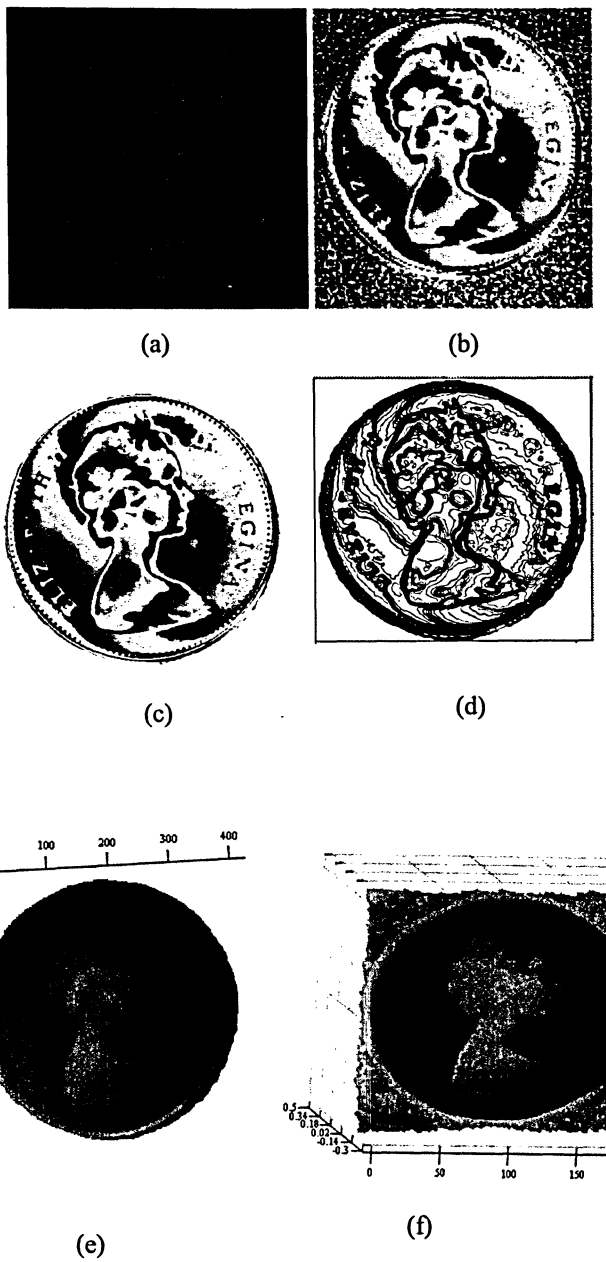

Fig.3.14 Surface topography of a Canadian quarter-coin measured by phase shifted shadow moiré: (a) a typical 4-step phase shifted image; (b) phase diagram with background; (c) phase diagram with background removed; (d) 2-D surface contours; (e) 3-D surface topography plot with no background; (f) 3-D plot without applying boundary detection.

3.3 System calibration by image subtraction and grey-scale histogram

A new system calibration scheme is proposed and implemented into the system. The previous chapters discussed the term *system sensitivity* w and its importance to the measurement. The system sensitivity is usually obtained by calibration. Accurate determination of w is important also because it affects the accuracy of phase shifting, given that the amount of phase-shift is determined by that of the vertical movement of the moiré grating, which is usually a fraction of w. System calibration is needed whenever a new application calls for a re-arrangement of the optical setup. As discussed in Chapter 2, when the moiré grating moves up or down an amount equal to w, the fringe order N will increase or decrease by one order. Therefore in a system calibration, w is determined simply by recording the displacement of glass grating while observing the lateral shift of moiré fringes by one order. A conventional system calibration uses standard surfaces or gauge blocks with known shapes or ramps. As the glass grating is moved slightly up/down, the entire fringe pattern shifts in lateral directions. An example is illustrated by Fig.3.15. Image (a) is the original moiré fringe pattern of which the centre of a dark fringe is initially positioned to coincide with the tip of a reference arrow marked on the screen of the display monitor. Image (b) is the phase-shifted fringe pattern before 2π phase shift is reached. As can be observed, the centre of the dark fringe moves away from the tip of the arrow. The image (c) is 2π phase-shifted pattern and the centre of the adjacent dark fringe reaches the tip of the arrow again. A movement of the grating of w corresponds to a constant phase change of the fringe pattern of 2π, or one integer order of the fringe shift. As a result, the

conventional calibration process is delicate since it relies on an operator's visual identification of fringe centres to ensure accurate fringe shift of an integer order.

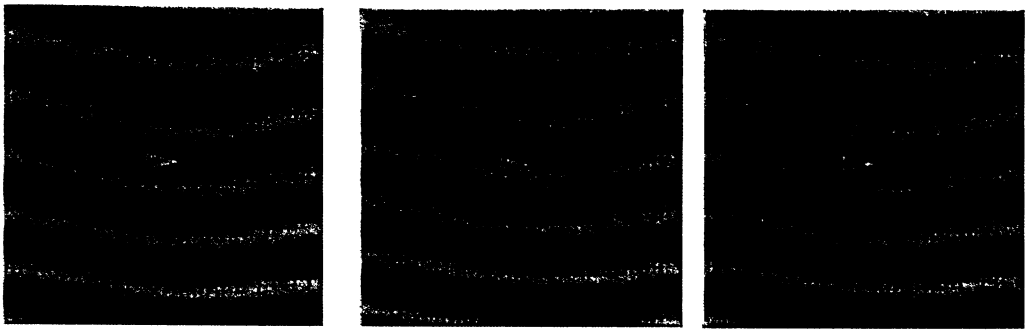

(a) (b) (c)

Fig.3.15 Conventional system calibration scheme.

And the calibration can be time consuming. To overcome these disadvantages, a new scheme is proposed to transform the human observation into a computer-automated process. As discussed in Chapter 2, the intensity function of moiré fringe pattern can be approximated by a sinusoidal function as follows:

$$I(x,y)=A(x,y)+B(x,y)\cos[\phi(x,y)] \qquad (3.9)$$

When a phase shift is introduced, the pattern changes but appears laterally shifted only since the terms A and B in the equation remain the same. With a constant phase shift of 2π, however, the intensity function becomes

$$I(x,y)=A(x,y)+B(x,y)\cos[\phi(x,y) \pm 2\pi] \qquad (3.10)$$

or becomes identical to Eq.3.9.

The proposed scheme determines the 2π phase shift based on a real-time subtraction of a phase-shifted fringe pattern, $g(x, y)$, from the original pattern $f(x, y)$. The subtraction yields an artificial image $h(x,y)$ as

$$h(x, y) = f(x, y) - g(x, y) \tag{3.10}$$

As $f(x, y)$ and $g(x, y)$ differ only by a constant phase equal to 2π, $h(x, y) = 0$ is reached and a full darkness will be exhibited on the screen. The darkness of the subtraction image $h(x, y)$ can be statistically evaluated and visualized with a pixel grey-level histogram also shown on the screen.

The probability of the occurrence of gray level r_k in the subtracted image is given by [64]

$$p_r(r_k) = \frac{n_k}{n} \qquad k = 0, 1, 2, \ldots, L\text{-}1 \tag{3.11}$$

where n is the total number of pixels in the subtracted image, n_k is the number of pixels at certain gray level r_k, and L is the total number of possible gray levels in the image. L is set to 256 for the current system. A live histogram, shown on the screen in real-time, is given by plotting $p_r(r_k)$ versus r_k. A histogram that shows $p_r(0) = 100\%$ will indicate that the full darkness or $h(x, y) = 0$ is reached. But that only theoretically occurs while in a practical application, due to various noises, the peak of the histogram of $h(x, y)$ stays close to 0. Therefore, the 2π phase shift is determined as the peak is moved closest to 0. Thus, the histogram nevertheless provides a quantitative and computer-automated judgement to the system calibration. As both the artificial image of subtraction and its pixel gray-value histogram are shown live, one can observe that the intensity distribution of $h(x, y)$ and the histogram vary with the continuous adjustment of the vertical position of the moiré grating. The system sensitivity w is equal to the corresponding amount of the grating motion when the 2π phase shift is determined based on the location of the peak of the histogram and

darkness of the subtracted image. It is worth noting that such a calibration test can be conducted on any surfaces.

Fig.3.16 (a) shows the original fringe patterns of a curved surface of an optical lens. (b), (c) and (d) illustrate the fringe patterns generated by subtracting another fringe pattern with π, $\pi/2$, and 2π phase shift, respectively. (d) appears the darkest and the peak of the histogram is the highest and closest to the vertical axis as compared with (b) and (c).

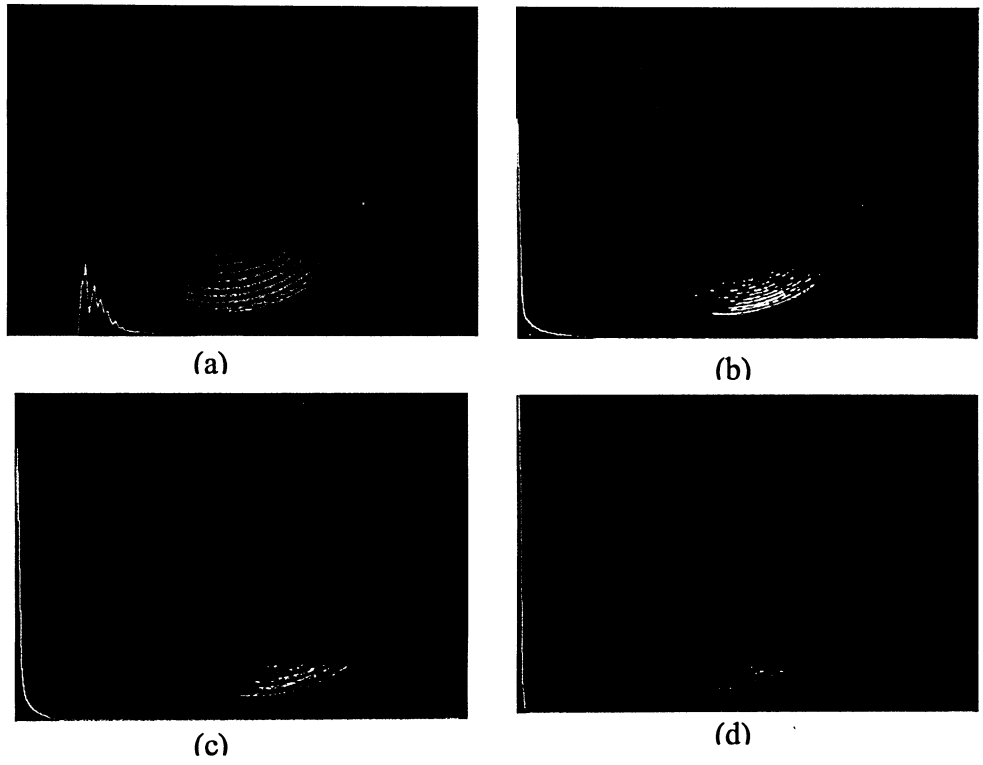

Fig.3.16 Determination of system sensitivity by a real-time image subtraction scheme: (a) an original fringe pattern; (b) an artificial image of subtraction of the fringe pattern with π phase shift from the original pattern; (c) subtraction of the fringe pattern with $\pi/2$ phase shift from the original pattern; (d) subtraction of the fringe pattern with 2π phase shift from the original pattern. A curve of the histogram is also shown in each image.

CHAPTER 4 SHADOW MOIRÉ DATA PRESENTAION

4.1 Need of new reference plane in data presentation

The purpose of applying shadow moiré to a surface is usually to measure the surface topography or to evaluate the surface out-of-plane displacement in relation to a load. In both cases, the application quantifies the degree that the surface deviates from a certain state of flatness. In the former application, it is the deviation from an ideal flat state and in the latter, from a previous state of the same surface.

As discussed in Chapter 2, shadow moiré measurement represents the distance from a surface point to the plane of the reference moiré grating. With strict requirements on the quality of the glass, a moiré grating usually can be fairly considered as a flat plane. Yet, since the measurements are given relative to the glass grating, the obtained topographic pattern of a surface becomes variable depending on how the surface is positioned with respect to the glass grating. Simply put, the moiré pattern of a surface varies as the surface tilts or moves under the grating. The classic way of result interpretation, as a quantity relative to the glass grating, may not always fit users' convenience and in some cases can be confusing. Instead, one would prefer that the presentation of the measurements be independent of the system alignment or any possible motion of the surface. To reach that end, a reference plane other than the plane of grating should be so chosen that it is common to all cases to facilitate the results interpretation. There are two practical choices of the reference planes: one being a plane passing through three corner points of the surface (or of the solution array), and the other a best-fit plane obtained from least square fitting the

raw measurements. The former choice is practically to affix a reference plane to the measured surface. With that, no change will be introduced between the surface and the reference plane when the surface tilts or shifts. Illustrated in Fig.4.1 is a surface depicted by a solid curve and its new position as plotted with a dashed curve. The motion, exaggerated from a normal case, can be the result of a surface re-positioning induced orientation change (e.g., changes in support condition), or deformation related. Once such a reference plane is established, a transformation of the originally measured data into the new reference system is necessary. The related mathematic process will be discussed in detail in the section to follow.

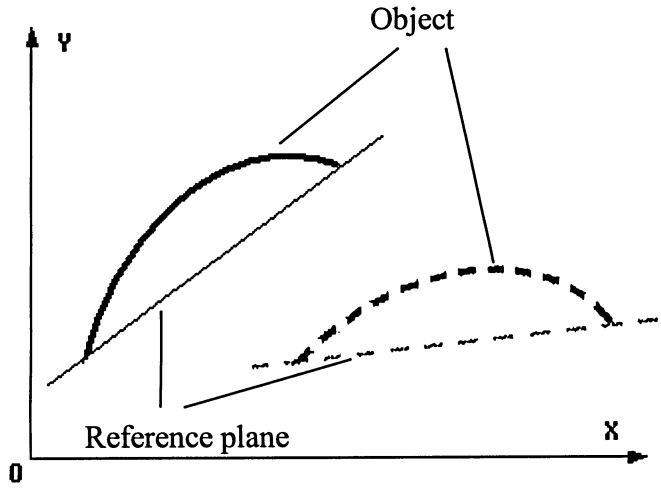

Fig.4.1 Two-Dimensional data normalization to eliminate effect of rigid body motion.

4.2 Reference plane determined by three corners of the surface

A new reference plane is introduced as follows, which is determined based on three points of the measured surface. The raw warpage measurement is then converted to yield warpage data with respect to the new reference plane.

Referring to Fig. 4.2, let $z = f(x, y)$ be a surface extended in x and y direction but warped with very small magnitude in its third dimension z. In a surface topographic measurement by shadow moiré, the coordinate plane x-o-y represents the reference grating and $z = f(x, y)$ is the original shadow moiré measurement. Let the three corner points of the warped surface be (x_1, y_1, z_1), (x_2, y_2, z_2) and (x_3, y_3, z_3), where z_1, z_2 and z_3 are the warpage data at the respective in-plane coordinate points (x_1, y_1), (x_2, y_2) and (x_3, y_3).

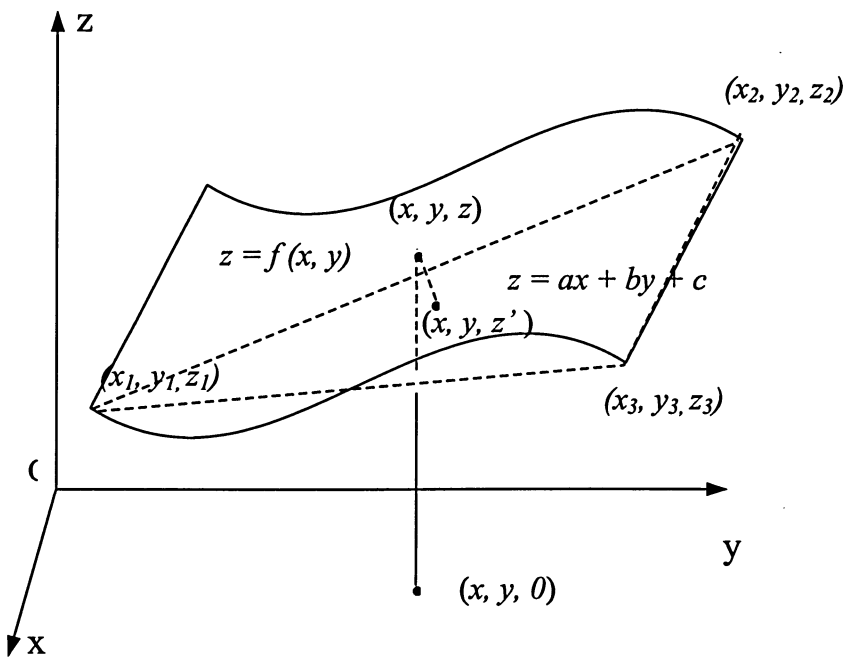

Fig. 4.2 New reference plane determined by three corner points of the surface being measured.

A plane in an *x*-*y*-*z* space is mathematically represented by

$$Z = ax + by + c \tag{4.1}$$

where *a*, *b* and *c* are constants. Knowing the three points (x_1, y_1, z_1), (x_2, y_2, z_2) and (x_3, y_3, z_3), the plane passing through them are determined by solving for the constants *a*, *b* and *c* from the simultaneous equations as follows:

$$\begin{aligned} z_1 &= ax_1 + by_1 + c \\ z_2 &= ax_2 + by_2 + c \\ z_2 &= ax_3 + by_3 + c \end{aligned} \tag{4.2}$$

The solutions are given as

$$\begin{aligned} a &= \frac{r(z_3 - z_2) - (z_2 - z_1)}{r(x_3 - x_2) - (x_2 - x_1)} \\ b &= \frac{(z_2 - z_1) - a(x_2 - x_1)}{y_2 - y_1} \\ c &= z_1 - ax_1 - by_1 \end{aligned} \tag{4.3}$$

where *r* is a constant and $r = \frac{y_2 - y_1}{y_3 - y_2}$.

In applications, a measured area is often rectangular shaped, and thus to chose three corners of the area as the above points is convenient. The conditions as follows are not to be neglected, noting that the denominators in Eq.4.3 must be nonzero:

$$\begin{aligned} r(x_3 - x_2) &\neq (x_2 - x_1) \\ y_2 &\neq y_1 \\ y_3 &\neq y_2 \end{aligned} \tag{4.4}$$

As noted, the z-coordinate of the point (x, y, z) in the surface $z = f(x, y)$ represents the directly measured warpage for a point $(x, y, 0)$. In the meantime, the same warpage with respect to the new reference plane is defined as the distance from the point (x, y, z) to the new reference plane, which is approximately equal to the line segment zz'. Denote the distance by D, the new warpage can be calculated with the following equation [65]:

$$D = \frac{ax + by + c - z}{\sqrt{a^2 + b^2 + 1}} \tag{4.5}$$

The above process is referred to as warpage data normalization. With such a transformation, the data obtained from the same surface measured with different moiré systems, or multiply probed in a time sequence, will be comparable since they can be presented with respect to a common reference plane. Fig.4.3 (a) shows a surface profile before and after 3-point plane normalization.

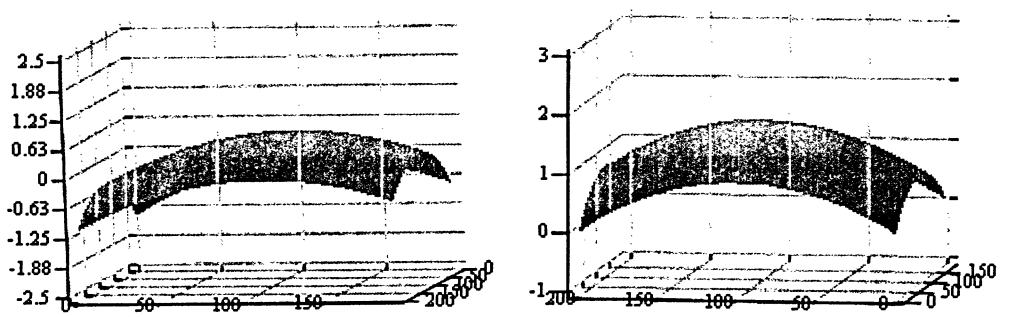

(a) (b)

Fig. 4.3 (a) Surface profile before 3-point plane normalization
(b) Surface profile after 3-point plane normalization.

4.3 Best fit plane

The best-fit plane is another reference plane proposed for the same purpose. The plane is the one that statistically best-fits the raw measurements in the sense that the areas above and below the plane are equal and kept to a minimum separation. The method of least squared error [38] is a common approach to determine the best-fit plane.

The squared error is the sum of the squared differences between sample data and the expected values as predicted by a specific function. The parameters that minimize the squared error are referred to as the best estimate. The simple example in Fig.4.4 illustrates how least square method can best fit a straight line into a set of samples of the size n (x_i, y_i), $i = 1, \ldots n$. Given a line with the function

$$f(x) = ax + b \tag{4.6}$$

where a is the slope, and b the y-intercept. The values of the constant a and b are determined if the line minimizes the square error.

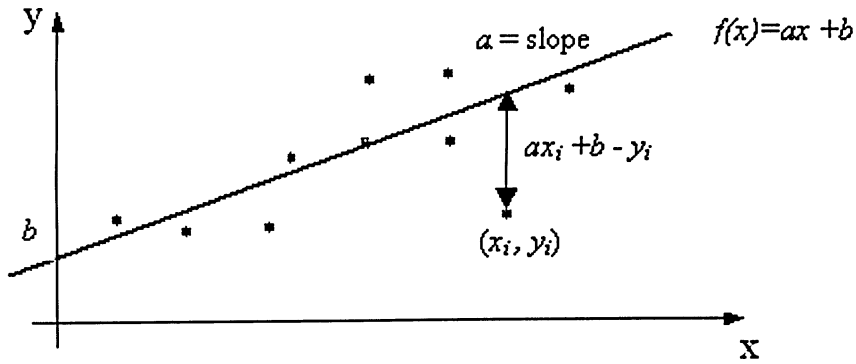

Fig.4.4 Least-Square best fitting for straight line.

The least square error E is defined as

$$E = \sum_{i=1}^{n} (ax_i + b - y_i)^2 \tag{4.7}$$

where n is the number of total samples.

The error function will have a minimum as the first derivatives with respect to a and c are 0:

$$0 = \frac{\partial E}{\partial a} = \sum_{i=1}^{n} 2x_i(ax_i + b - y_i)$$

$$0 = \frac{\partial E}{\partial b} = \sum_{i=1}^{n} 2(ax_i + b - y_i) \tag{4.8}$$

Eq.4.8 can be re-organized in the following form

$$\left(\sum_{i=1}^{n} x_i^2\right)a + \left(\sum_{i=1}^{n} x_i\right)b = \sum_{i=1}^{n} x_i y_i$$

$$\left(\sum_{i=1}^{n} x_i\right)a + nb = \sum_{i=1}^{n} y_i \tag{4.9}$$

a and b are solved with Equation (4.9) and the best-fit line is thus determined.

To extend the above into a two dimensional case, a best-fitting plane can be obtained with the function

$$f(x, y) = ax + by + c \tag{4.10}$$

The least square error E is defined as

$$E = \sum_{i=0}^{n-1} (ax_i + by_i + c - z_i)^2 \tag{4.11}$$

And the zero partial derivatives of the equation with respect to *a*, *b*, and *c* are given as

$$0 = \frac{\partial E}{\partial a} = \sum_{i=1}^{n} 2x_i(ax_i + by_i + c - z_i)$$

$$0 = \frac{\partial E}{\partial b} = \sum_{i=1}^{n} 2y_i(ax_i + by_i + c - z_i)$$

$$0 = \frac{\partial E}{\partial c} = \sum_{i=1}^{n} 2(ax_i + by_i + c - z_i) \qquad (4.12)$$

Eq.4.12 yields the following equations to find the best-fit parameters *a*, *b* and *c*:

$$\left(\sum_{i=1}^{n} x_i^2\right)a + \left(\sum_{i=1}^{n} x_i y_i\right)b + \left(\sum_{i=1}^{n} x_i\right)c = \sum_{i=1}^{n} x_i z_i$$

$$\left(\sum_{i=1}^{n} x_i y_i\right)a + \left(\sum_{i=1}^{n} y_i^2\right)b + \left(\sum_{i=1}^{n} y_i\right)c = \sum_{i=1}^{n} y_i z_i$$

$$\left(\sum_{i=1}^{n} x_i\right)a + \left(\sum_{i=1}^{n} y_i\right)b + nc = \sum_{i=1}^{n} z_i \qquad (4.13)$$

Fig.4.5 below shows the results before and after best-fit plane normalization.

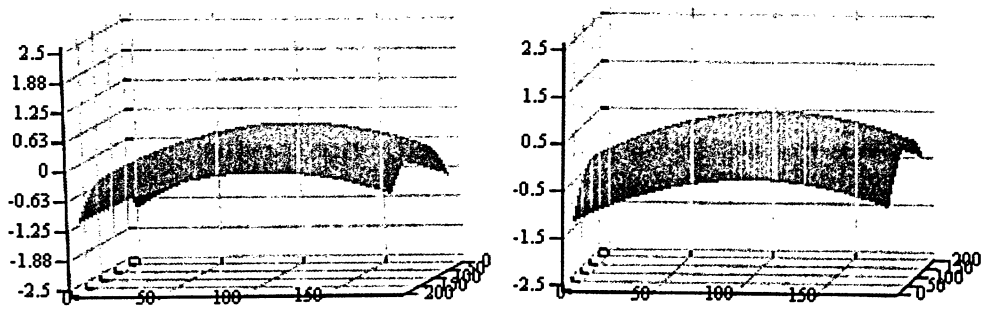

(a) (b)

Fig. 4.5 (a) Surface profile before best-fit plane normalization
(b) Surface profile after best-fit plane normalization.

4.4 Comparison of the two reference planes

The data normalization with the three-point reference plane is simple and computation inexpensive. The program can easily find three corner points of a surface to determine the reference plane. The least square reference plane is determined by calculating the summations in Eq.4.13, which is time consuming, especially when the phase array is large in size.

For tests including a series of measurements conducted on the same surface, the selections of three corner points must be kept consistent to maintain the same resultant reference plane for all measurements taken at different time instants. Meanwhile, extra caution is recommended to avoid picking a noisy corner point since, otherwise, an incorrect reference plane will result. Furthermore, for a test that involves a non-rectangular shaped surface, to select which three points is challenging to the program. In that case, an interactive process may be required to manually select the three corners.

Compared to 3-corners normalization, the best-fitting normalization is a global and automatic process that is less vulnerable to the noisy points often existing in a phase array. And the best-fit method does not impose limit on the shape of the sample; therefore, it normally requires no manual selection of corner points.

CHAPTER 5 VERIFICATION AND APPLICATIONS OF THE NEW SHADOW MOIRÉ TECHNIQUE

5.1 Verification tests

Verification tests are conducted using the experimental setup schematically shown in Fig.2.3. A recording CCD camera with a medium pixel resolution is positioned vertically while an incandescent light source provides the illumination with an incident angel of near 45°. A glass grating of 20 lines/mm was mounted on a micromotion stage to allow easy adjustment of the grating's vertical and in-plane position, as well as the out-of-plane tilts. Such adjustments are necessary not only for the realization of phase shifting but also for optimizing the quality (such as the contrast) of the fringe patterns. For surfaces that warp during a test due to deformation, the grating position relative to the surface should be adjusted in-between consecutive measurements to make sure that no parts of the surface is in contact with the grating. A program flow chart is given in Appendix 1.

Previous studies [11,24,37] claimed that the phase shifting technique as applied to fringe analysis can be used to achieve a resolution as high as 1/100 fringe sensitivity. For the current setup with a grating of 20 lines/mm and an illumination angle of 45°, the fringe sensitivity w is 50 μm. Therefore the resolution should reach 1/100 fringe pitch or 0.5 μm according to the theory. In practical applications, the inaccuracy in system parameters and the image noise will normally cause reduction in the measurement accuracy. A new measurement system is usually assessed in a verification test and the results are compared with those obtained using an independent and established technique. In this study, a two-

stage flat is used as a test sample, as sketched in Fig.5.1 (a). The test is aimed to measure the height of the step in the middle of the block. A fringe pattern is shown in Fig.5.1 (b) in which a box in solid lines outlines the rectangular area to be analyzed. The shadow moiré measured three-dimensional surface profile is plotted in Fig.5.1(c). According to the diagram, the height of the step is 0.6070 mm. Meanwhile, a micro caliper is used as an independent check, which gives a reading of 0.610 mm. The difference is 0.003mm or 0.491%, as listed in Table 5.1.

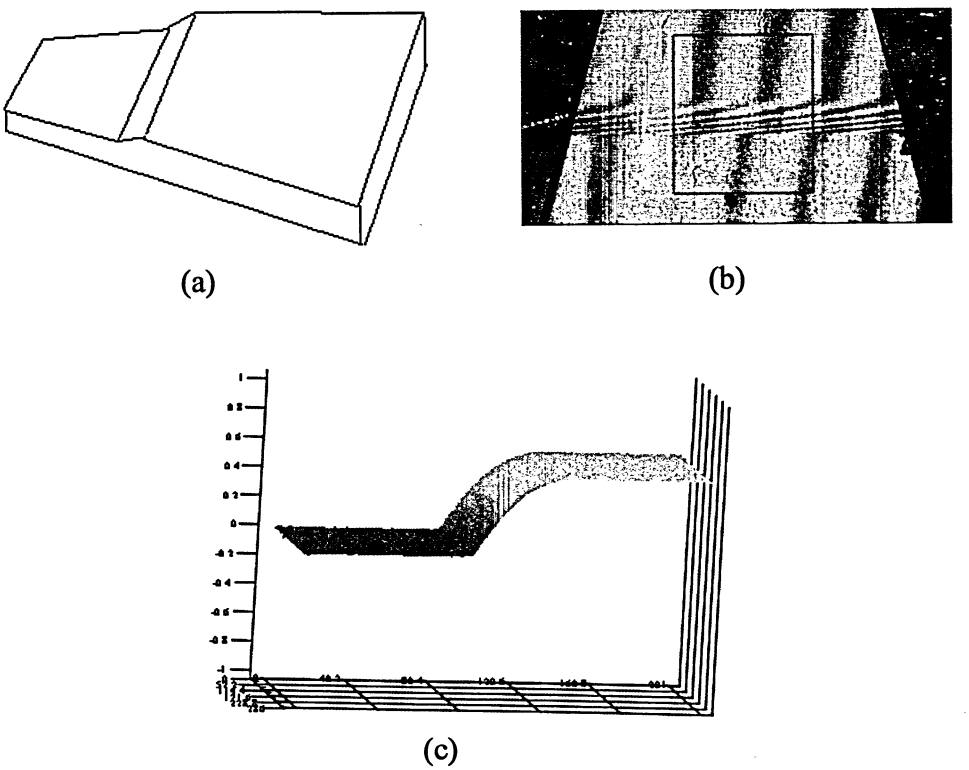

Fig.5.1 Experimental results for gage block measurement
(a) Schematic plot of a gage block (b) Gage block image with moiré pattern (c) 3-D surface profile.

Table.5.1 Shadow moiré result compared to that measured by Micro caliper.

Measurement	Step (mm)
Micro caliper	0. 610
Shadow Moiré	0. 6070
Difference (mm)	0. 0030
Difference (%)	0. 491

5.2 A typical application to microelectronics

The scope of the application is to quantitatively study the warpage behavior for freestanding BGA (Ball Grid Array) packages, bare PCBs (Printed Circuit Board) and their assembled units, as schematically shown in Fig.5.2. The planarity of the parts and the co-planarity between the component and the board and the respective variations in responding to a predefined temperature profile are the focus of the study. The data are critical for the reliability analysis of large-size BGA assemblies. The per-package I/O pin-counts of these units can be in excess of 2,000.

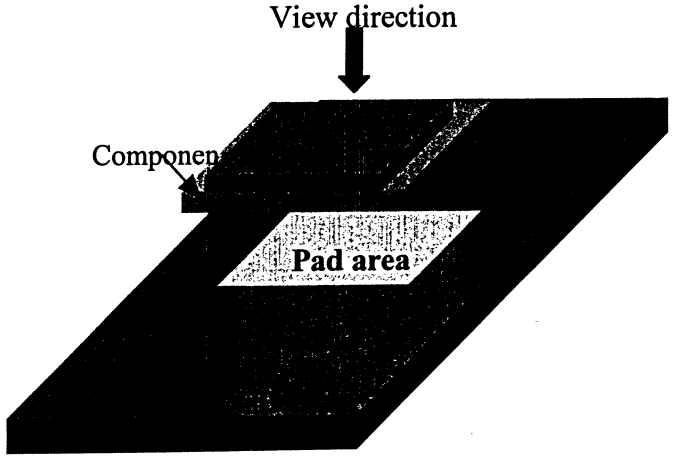

(a) 3-D view of BGA and PCB

Fig.5.2 Schematic diagram of BGA and PCB assembly.

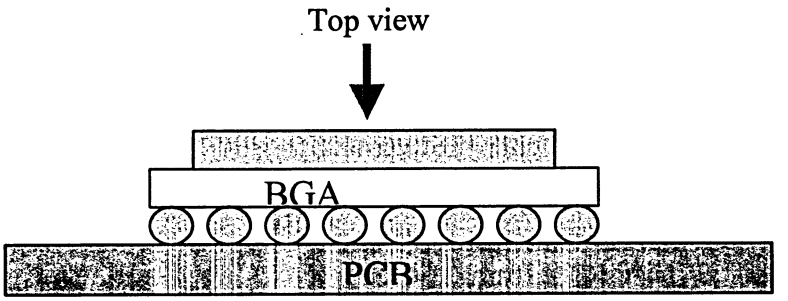

(b) Top view of BGA and PCB

Fig.5.2 (continued).

The tests are conducted using the same system as used in the verification test. In a typical application, the room temperature warpage is evaluated first and the measurements are then taken at approximately every 20 °C as the temperature is heated up until 245 °C in simulating a solder joint reflow environment (Fig. 5.3). It is noted that the melting point of a typical lead-free solder is around 230 °C. The warpage measurement continues during the cooling period and repeats several times at the room temperature after cooling is completed.

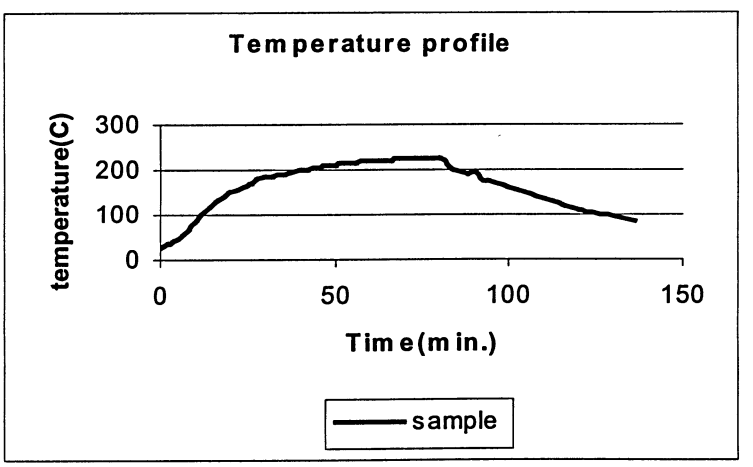

Fig. 5.3 BGA temperature vs. time.

Fig.5.4 shows the three-dimensional surface profiles and two-dimensional contour maps that demonstrate the warpage variations with temperature for the freestanding parts, as well as the assembly units. For PCBs, the measurement is concentrated in the copper-pad areas and, for BGA components, the substrates where the solder bumps are laid. The measurement reveals that two types of warpages exist. The centrically warped shape is regularly found in BGA substrates and PCB of assembled units. But skewed or wavy shaped warpage is shown quite often for bare PCBs due to PCB manufacturing and segmentation/partitioning. The thermal warpage causes reduced co-planarity between the BGA substrate and PCB pad area, which is critical to BGA assembling process. When such co-planarity is compromised, the solder joint standoff (the height) will vary from a package's central to peripheral area. Solder joints with high standoff tend to experience high stresses upon solder solidification as the assembly cools down from the reflow temperature. On the other hand, the shorter joints have more chances to become bridged with the neighboring joints. High temperature tends to increase the warpage of a PCB, but only mildly affects the ceramic-made BGA due to its high thermal rigidity. As a thermal cycle is completed, the warpage of a freestanding PCB will not recover as the ceramic substrate does, as shown in Fig.5.5, due to viscosity of the plastic material that a PCB is largely made of. Residual warpage can remain for a period as long as a few weeks, though a part of that is visco-plastic and becomes permanent. Compared with that in a bare PCB, warpage in the pad area of an assembly unit is much higher cooling back to the room temperature. It is noted that as the temperature drops below the solder melting point during a solder reflow cycle, the solder joints become solidified so that the component and the

PCB are interconnected. With the joints, the difference in the CTE (coefficient of thermal expansion) mismatch between the plastic PCB and the ceramic BGA substrate takes effect. As a result, the solder joints are subjected to process induced residual stress that in turn exerts bending on the PCB underneath the solder joints, exhibited as severer warpage at the room temperature. More experimental tests can be found in Appendix.2.

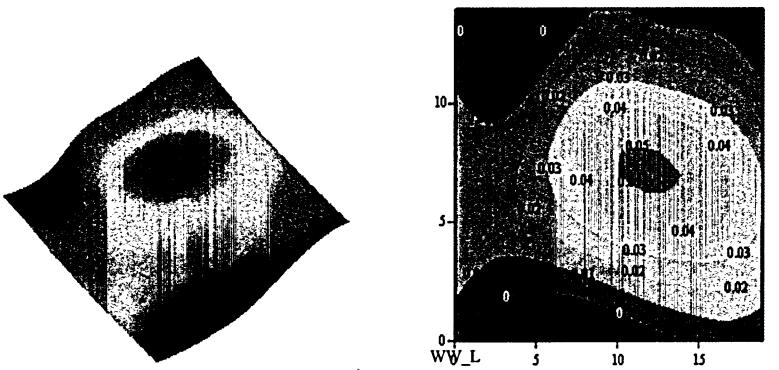

(a1) Warpage of BGA at 24°C (mm)

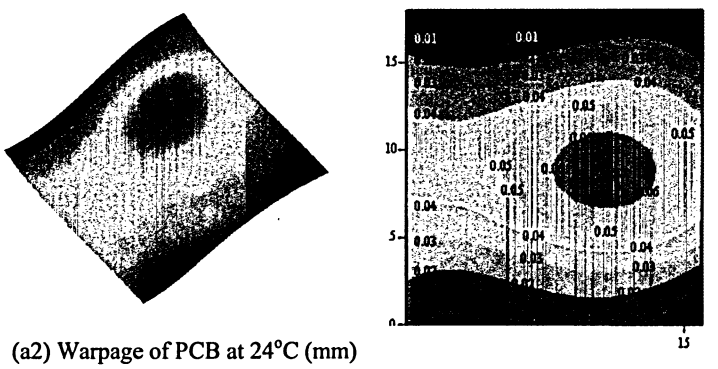

(a2) Warpage of PCB at 24°C (mm)

Fig.5.4 BGA and PWB warpage at different temperature.

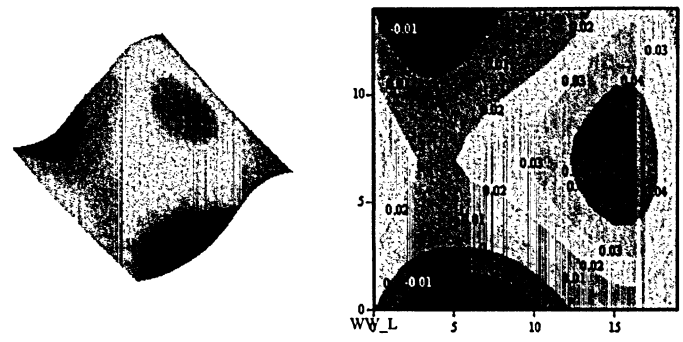

(b1) Warpage of BGA at 150°C Ramp Up(mm)

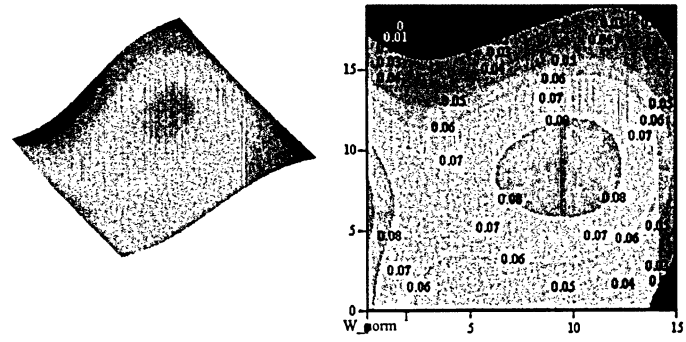

(b2) Warpage of PWB at 150°C Ramp Up(mm)

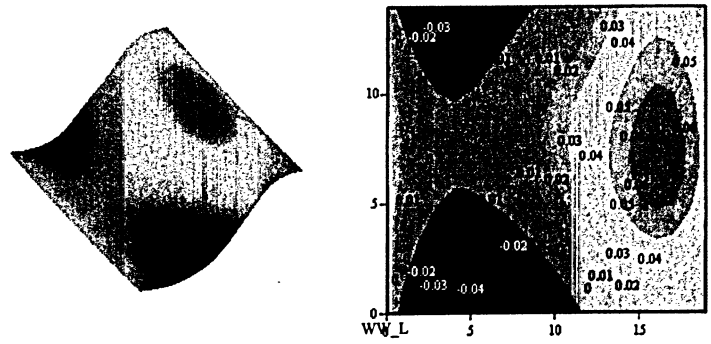

(c1) Warpage of BGA at 245°C Ramp Up(mm)

Fig.5.4 (continued).

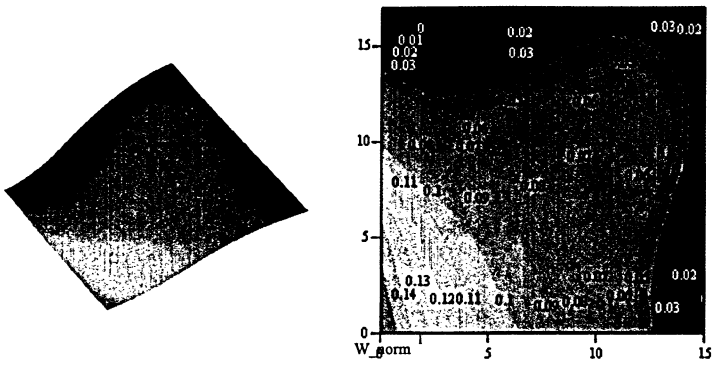

(c2) Warpage of PWB at 245°C Ramp Up(mm)

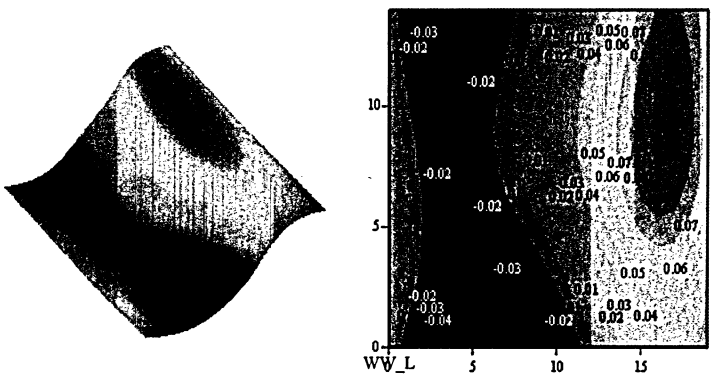

(d1) Warpage of BGA at 155°C Ramp Down(mm)

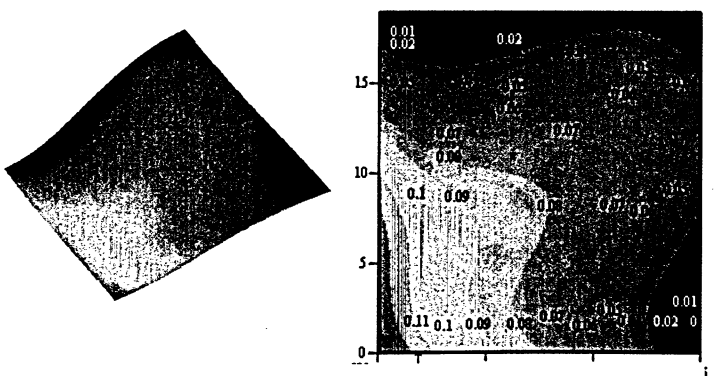

(d2) Warpage of PWB at 155°C Ramp Down(mm)

Fig.5.4 (continued).

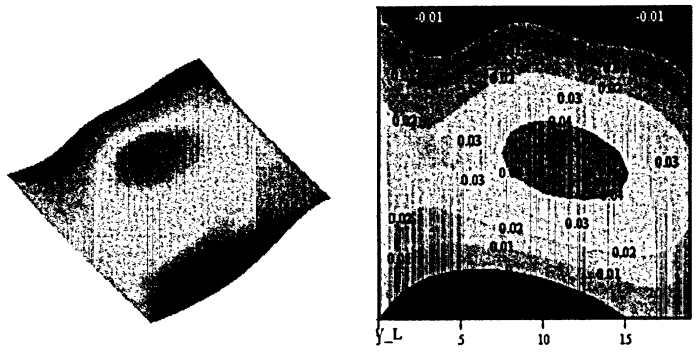

(e1) Warpage of BGA at 22°C Ramp Down(mm)

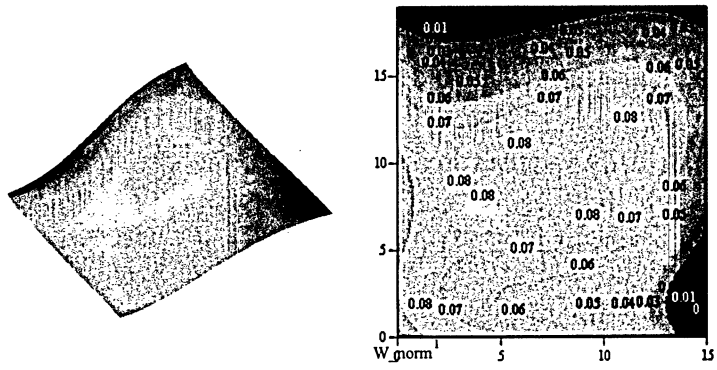

(e2) Warpage of PWB at 30°C Ramp Down(mm)

Fig.5.4 (continued).

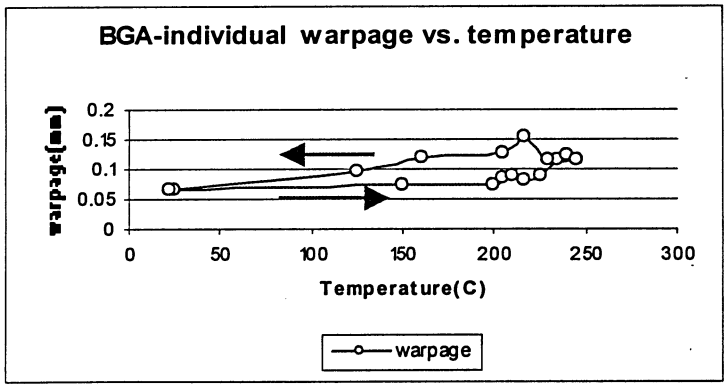

(a) Warpage plot of BGA vs. Temp.

Fig.5.5 Warpage of BGA and PWB during the reflow process.

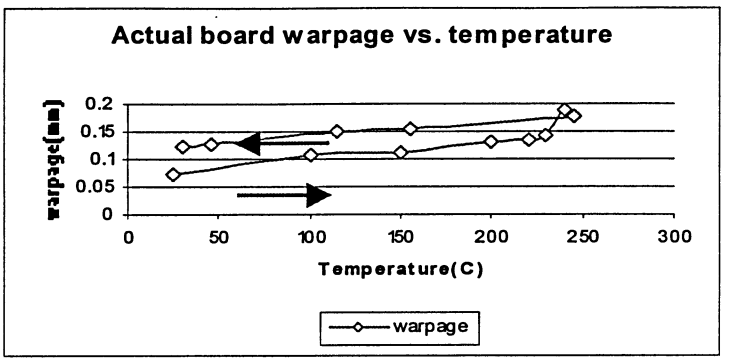

(b) Warpage plot of PWB vs. Temp.

Fig.5.5 (continued).

5.3 Error analysis

Errors in shadow moiré measurements could result from several different sources including the heat flow and electronically induced image distortion, the environment vibration, the system calibration error, the light intensity variation and the angle of divergence of the illumination, etc. By means of averaging and filtering the multiply captured images, the image distortion may be reduced. To sit the shadow moiré system on a vibration-free optical table can reduce the impact of environmental instability. And the proposed calibration scheme effectively increases the accuracy of the system sensitivity. What remains is the non-collimated light source that is likely the dominant source of error. Though the use of collimated light gives a constant illumination angle to eliminate the measurement error, a non-collimated light source is commonly employed for its relative simplicity and flexibility, as well as low cost. The errors induced by illumination divergence can be effectively reduced by placing the light source and camera at the same height from the surface of object, as discussed in Chapter 2. However, in some cases in which high-contrast fringe patterns are needed, the light source may be positioned at

different heights/positions from where the camera is located. The error analysis for the cases is described as follows.

Fig.5.6 illustrates the effect of light divergence when a non-collimated light is used in the system for sample illumination. Assuming a normal viewing configuration so that the observation angle α in Equation (2.1) is zero. The illumination angle β, however, varies from point to point on the surface. As shown in Fig.5.6, β_1 and β_2 are the actual angles of illumination at the left and right edges of surface, respectively. From Eq.2.2, W at the leftmost point is

$$W_l(x,y) = N(x,y)p / \tan\beta_1 \qquad (5.1)$$

And W at the rightmost point is

$$W_r(x,y) = N(x,y)p / \tan\beta_3 \qquad (5.2)$$

Though the error is obvious, it can be minimized if the light source is placed so far away from the surface that the difference in tanβ becomes negligible.

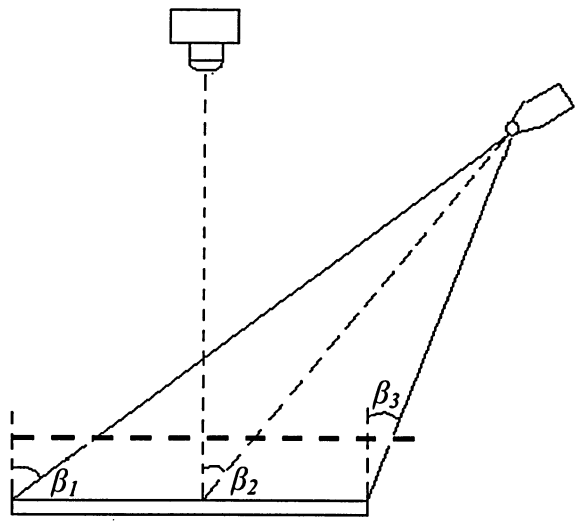

Fig.5.6 Analysis of shadow moiré measurement error caused by using a point light source.

CHAPTER 6 CONCLUSIONS

The shadow moiré method is studied and new fringe processing algorithms are introduced to achieve computer automated surface profiling. The main achievements of this research include the following aspects and the program flow chart is shown in the Appendix.1.

(1) A new algorithm of phase unwrapping is studied and introduced.

Phase unwrapping is a key to realizing the phase-shifting and in turn, the automated measurement. Based on a study of different algorithms, the research eventually focuses on a multi-grid least-square unwrapping algorithm. Compared with the commonly applied FFT and DCT algorithms, the multi-grid unwrapping algorithm, when incorporated into shadow moiré, has an advantage of being more time-efficient in fringe processing and less restrictive on the size of data array. The implementation of the new unwrapping algorithm has also led to improved resolution of the measurement owing to the enhanced capability of resolving image local details. The study shows that the resolution of the new system can reach a small percentage of the system sensitivity that is defined by the classic shadow moiré method. Both three-step and four-step phase shifting algorithms are studied and implemented. A comparison of the results obtained based on the same test shows that the relative difference is less than 0.1% in the phase-angles.

(2) An automated system calibration scheme is proposed and realized.

The conventional system sensitivity is calibrated using gauge blocks or surfaces of known shapes. Such a calibration is usually a time consuming process and relies heavily on an

operator's observations. Utilizing the fringe pattern phase-shifting mechanism, in combination with a real-time digital image subtraction and a histogram of the subtraction, the proposed new scheme automates the determination of the system fringe sensitivity. In addition, it has realized a convenient feature of the calibration by which the test can be performed on any surfaces instead of using a standard gauge block.

(3) A contour detection technique in fringe processing is incorporated.

This technique facilitates the measurement for non-rectangular or irregular shaped surfaces, as well as hollow surfaces. The new system implemented with edge detection automates the distinguishing of the surface being measured from its boundaries. The fringe analysis can now be limited to within the boundaries of the surface. Moreover, the separation of the surface from its background facilitates the reading and interpretation of phase diagrams. In an application, the quality of a phase diagram is important to the reliability of the final measurements. The better efficiency, accuracy and resolution due to the implementation of the boundary detection technique are demonstrated in the applications to measuring topography for a round shaped area and a hollow section.

(4) A data normalization procedure is introduced to eliminate the effect of rigid body motion on the data interpretation.

This research has studied and proposed a three-corner-point plane as well as a best-fit plane, as the reference plane, and procedures to transform the originally obtained warpage data to the new reference plane. The original shadow moiré measurement is determined in

reference to a plane that is in parallel to the plane of the glass grating of the moiré system. The so-called data normalization is in essence a mathematical procedure that converts the original data to be presented in a different reference plane. The new reference plane is attached to the surface being measured. As a result, the measurements obtained from a surface can be presented without being affected by the change of surface position relative to the shadow moiré system.

(5) Noise reduction techniques are introduced into the new system.

The image noise and its impact on the fringe analysis as well as noise reduction techniques are studied. The introduction of noise reduction techniques into the new system has resulted in improved quality of phase diagrams and better accuracy of the measurements. The elimination or significant reduction of spike noise is especially imperative to the establishment of a three-corner point reference plane.

REFERENCES

[1] Daniel Post, Bongtae Han and Peter Ifju, "High Sensitivity Moiré: Experimental Analysis for Mechanics and Materials," pp. 86-96, 118-129,419-426 (1994)

[2] James W. Dally, William F. Riley, "Experimental Stress Analysis," Second Edition, pp380-4397, (1978)

[3] Pericles S Theocaris, "Moiré Fringes in Strain Analysis," pp.20-39 (1969)

[4] Hai Ding, Reinhard E.Powell, Carl R.Hanna and Charles Ume, "Warpage Measurement Comparison Using Shadow Moiré and Projection Moiré Methods," *IEEE Transactions on Components and Packaging Technologies*, Vol. 25, No. 4, pp. 714-721 (2002)

[5] K. Creath and J. C. Wyant ,"Moiré and Fringe Projection Techniques," Optical Shop Testing, Second Edition, pp. 653-684 (1992)

[6] Gregory J. Petriccione and I. Charles Ume, "Warpage Studies of HDI Test Vehicles During Various Thermal Profiling," *IEEE Transactions on Advanced Packaging*, Vol. 22, No. 4, pp.624-637 (1999)

[7] Gerard Mauvoisin, Fabrice Bremand, and Alexis Lagarde, "Three-dimensional shape reconstruction by phase-shifting shadow moiré," *Applied Optics*, Vol. 33, No.11, pp. 2163-2169 (1994)

[8] Toru Yoshizawa, and Teiyu Tomisawa, "Shadow moiré topography by means of the phase-shift method," Optical Engineering, Vol.32, pp.1668-1674 (1993)

[9] C.P.Yeh, K.Banerjee, T.Martin, C.Umeagukwu,and R.Fulton, "Experimental and Analytical Investigation of Thermally Induced Warpage for Printed Wiring Boards," in Proc. IEEE 41th Electronic Component Technology Conference, pp.382-387 (1991)

[10] Kaushal Verma, Derek Columbus, and Bongtae Han, "Development of Real Time/Variable Sensitivity Warpage Measurement Technique and its Application to Plastic Ball Grid Array Package," *IEEE Transactions on Electronics Packaging Manufacturing*, Vol. 22, No.1, pp.63-70 (1999)

[11] Yinyang Wang and Patrick Hassel "On-line Measurement of Thermally induced Warpage of BGAs with High Sensitivity Shadow Moiré" *Int. J. Microcirc. Electron. Packag.*, Vol. 21, No. 2, pp. 191–196, (1998)

[12] Dawei Zheng, Ray P.Hwang,Xinyu Dou , Chaopin Yeh "Warpage Analysis of 144-Pin TQEF During Reflow Using Image Processing," *Electronic Components and Technology Conference*, pp.1176-1181 (1997)

[13] A.J.Durelli and V.J.Parks "Moiré Analysis of Strain" pp. 16-23 (1970)

[14] Stephen J Marshall, Robert Rixon, Donald N Whiteford and James T Cumming, "The Orthoform 3-Dimensional Clinical Facial Image System," *Proc. Int. Fed. Hosp. Eng.* Congress 15, pp.83-87 (1998)

[15] Chwei Goong Tseng and Yuan Show Jiang "Optical interference dilatometer," *Measurement Science and Technology*, Vol.16, pp.2114-2120 (2005).

[16] L D'Acquisto, L Fratini and A M Siddiolo, "A modified moiré technique for three-dimensional surface topography," *Measurement Science and Technology*, Vol.13, pp.613-622 (2002)

[17] Kieran G. Larkin, "A self-calibrating phase-shifting algorithm based on the natural demodulation of two-dimensional fringe patterns," *Optics Express*. Vol.9, pp.236-253 (2001)

[18] J. Degrieck, W. Van Paepegem, P. Boone, "Application of digital phase-shift shadow Moiré to micro deformation measurements of curved surfaces," *Optics and Lasers in Engineering* Vol.36 pp.29-40 (2001)

[19] Winfried Haas, "Application of Moiré Topography to small objects in palaeontology and sedimentology," *Geol. Mag.* Vol.135, pp. 93-99, (1998)

[20] Chao-Pin Yeh, Charles Ume, Robert E. Fulton, Karl W. Wyatt, and John W. Stafford, "Correlation of Analytical and Experimental Approaches to Determine Thermally Induced PWB Warpage," IEEE *Transactions on Components, Hybrids, and Manufacturing Technology*, Vol. 16, No. 8, pp.986-995 (1993)

[21] J.E.A Liao and A.S.Voloshin, "Enhancement of the Shadow-moiré Method Through Digital Image Processing," Experimental Mechanics, pp.59-64 (1992)

[22] Kuo-Shen Chen, Terry Yuan-Fang Chen, Chia-Cheng Chuang, and I.-Kuan Lin, "Full-Field Wafer Level Thin Film Stress Measurement by Phase-Stepping Shadow Moiré," IEEE *Transactions on Components and Packaging Technologies*, Vol. 27, No. 3, pp.594-601 (2004)

[23] Michael R. Stiteler, I. Charles Ume, and Brian Leutz, "In-Process Board Warpage Measurement in a Lab Scale Wave Soldering Oven," IEEE *Transactions on Components, Packaging and Manufacturing Technology*, Part A, Vol.19, No. 4, pp.562-569 (1996)

[24] Hai Ding, I. Charles Ume, Jian Zhang, and Daniel F. Baldwin, "Integrated Hardware and Software for Improved Flatness Measurement With ATC4.1 Flip-Chip Assembly Case Study," IEEE Transactions on Instrumentation and Measurement, Vol. 54, No. 5, pp.1898-1904 (2005)

[25] M. Heredia Ortiz and E.A. Patterson, "Location and Shape Measurement Using a Portable Fringe Projection System," *Society for Experimental Mechanics*, Vol.45, No.3 pp.196-204 (2005)

[26] A. Moreno Years, "Moiré topography in odontology," *Optics and Lasers in Engineering,* Vol.40 , pp.143–152 (2003)

[27] O. Fernandez, "Obtaining a best fitting plane through 3D georeferenced data," *Journal of Structural Geology,* Vol.27, pp.855–858 (2005)

[28] C. Quan, Y. Fu, C.J. Tay, "Determination of surface contour by temporal analysis of shadow moiré firnges," Optics Communications, No.230, pp.23-33 (2004)

[29] Anh X. H. Dang, I. Charles Ume, and Swapan K. Bhattacharya, "Process Induced Warpage in Multitiled Alumina Substrates for Large Area MCM-D Processing," IEEE *Transactions on Advanced Packaging*, Vol. 23, No. 3, pp. 436-446 (2000)

[30] Mike Dickersons, Lothar Klein, Giedrius Liutkus, John Messina
Dirk Zwemer, Manas Bajaj, Russell Peak, Thomas Thurman, Kevin Brady, S. McCarron, A. Spradling, "PWB Warpage Analysis and Verification using an AP210 Standards-based Engineering Framework and Shadow Moiré," *5th. Int. Conf: on Thermal and Mechanical Simulation and Experiments in Micro-electronics and Micro-Systems, EuroSimE2001*, pp.121-131 (2001)

[31] Lord Rayleigh, Philos. Mag. No.47, pp.193 (1874)

[32] Yatagai, T. and M. Idesawa, "Automatic Fringe Analysis for Moiré Topography," Opt. Lasers Eng., 3(l), pp.73-83 (1982)

[33] Dirckx J.J.J., Decraemer W.F., Dielis M.M.E., "A phase shift method based on object translation for full field automatic three dimensional surface reconstruction from moiré topograms," Applied optics, Vol.27, No.6, pp.1164-1169 (1988)

[34] Meadows D M, Johnson W O and Allen J B, "Generation of surface contours by moiré patterns," Applied Optics, Vol. 9 pp.942–947 (1970)

[35] H. Takasaki, "Moiré topography", Applied Optics, Vol. 9, pp.1467-1472 (1970)

[36] Wasowski, "Moiré Topographic Maps," Optical Communications, Vol. 2, No. 7, pp. 321-323 (1970).

[37] Zhaoyang Wang, "Development and Application of Computer-Aided Fringe Analysis," Dissertation, Department of Mechanical Engineering, University of Maryland, College Park, MD, USA (2003)

[38] Donald Trim, "Calculus for Engineers," pp.1054-1060 (1998)

[39] T. W. Ng, A. Tajuddin, "Shadow moiré topography using a flatbed scanner," *Optics Engineering*, Vol.41, pp.1908–1911 (2002)

[40] A. K. Maji and M. A. Starnes, "Shape Measurement and Control of Deployable Membrane Structures," *Experimental Mechanics,* Vol. 40, No. 2, pp.154-159 (2000)

[41] M.M. Ratnam, J.H. Lim and H.P.S. Abdul Khalil, "Study of Three-dimensional Deformation of a Pallet Using Phase-shift Shadow Moiré and Finite-element Analysis," *Experimental Mechanics,* Vol. 45, No. 1,pp.9-17 (2005)

[42] Iqbal Marie, Hisham Qasrawi, "Virtual assembly of pottery fragments using moiré surface profile measurements," *Journal of Archaeological Science* Vol.32 pp.1527-1533 (2005)

[43] Wu, J.C.L., Han Hien Shine, Sting Wu, Mike Hung and Lee, J.J, "Study of rapid cure BGA mold compound on warpage with shadow moiré," IEEE, Electronic *Components and Technology Conference*, pp.708-713 (1999)

[44] Shoulung Chen, Tsai, C.Z., Kao, N. and Enboa Wu, " Mechanical behavior of flip chip packages under thermal loading," IEEE, *Electronic Components and Technology*, Vol. 2, pp.1677 - 1682 (2005)

[45] Jiunn Hsuh Lim, Mani Maran Ratnam, "Optical signal processing for shape measurement," IEEE, *Signal Processing and its Applications*, Vol.2, pp.454 - 457 (2001)

[46] Bansal S., Markondeya Raj, Shinotani K., Bhattacharya S., Tummala R., Lance M.J, "Reliability assessment of high density multi-layer board assembly using shadow Moire and luminescence spectroscopy," IEEE, *Electronics Packaging Technology Conference*, pp.126 – 132 (2002)

[47] Heredia-Ortiz, M., Patterson, E. A., "On the Industrial Applications of Moiré and Fringe Projection Techniques," Optics Communications, Vol.39, No.3, pp. 95-100 (2003)

[48] Han, B., Ifju, P., Post, D, "Geometric Moiré Methods with Enhanced Sensitivity by Optical/Digital Fringe Multiplication," Experimental Mechanics Vol. 33, No. 3, pp. 195 – 200 (1993)

[49] Kokidko, D., Gee, L., S. C. Chou, F. P. Chiang, "Method for measuring transient out-of-plane deformation during impact," International Journal of Impact Engineering, Vol. 19, No. 2, pp. 127-133 (1997)

[50] Virendra Jadhav, Scott Moore, Cheryl Palomaki and Son Tran, "Flip Chip Assembly Challenges Using High Density, Thin Core Carriers," IEEE, *Electronic Components and Technology Conference,* (2005)

[51] R. Zhao, H. Lu, M. Zhou, C. Sun, "Surface Profiling Using a Modified Shadow Moiré Technique," IEEE, *International Symposium and Exhibition on Advanced Packaging Materials* , pp.151-154 (2006)

[52] R. Zhao, H. Lu, M. Zhou, C. Sun, "Improved Shadow Moiré Method For Out-of-plane Displacement Measurement," Canadian Society for Mechanical Engineering (2006)

[53] Piks Inside, "Digital Image Processing," Third edition, pp. 260-266, 443-469, 566-580 (2001)

[54] Scott E Umbaugh, "Computer Imaging: Digital Image Analysis and Processing," pp.93-100, 135-143, 232-235, 415-426 (2005)

[55] Milan Sonka, Vaclav Hlavac, Roger Boyle "Image Processing, Analysis, and Machine Vision," pp.32-33, 35-37, 135-158 (1998)

[56] Dennis C. Ghiglia, Mark D.Pritt, "Two-Dimensional Phase Unwrapping: Theory, Algorithms, and Software," pp.100-122, 136-150, 178-247, 280-306(1994)

[57] Mark D.Pritt, Jerome S. Shipman, "Least-Squares Two-Dimensional Phase Unwrapping Using FFT's," IEEE *Transactions on Geoscience and Remote Sensing*, Vol.32, No.3, pp.706-708 (1994)

[58] D. C. Ghiglia and L. A. Romero, "Robust two-dimensional weighted and unweighted phase unwrapping that uses fast transforms and iterative methods," J. Optical Society of America A (Optics and Image Science) Vol.11, pp. 107-117, (1994)

[59] Anand Asundi and Zhou Wensen, "Fast phase-unwrapping algorithm based on a gray-scale mask and flood fill," Applied Optics, Vol.37, No.23, pp.5416-5420 (1998)

[60] Hong Zhao, Wenyi Chen, and Yushan Tan, "Phase-unwrapping algorithm for the measurement of three-dimensional object shapes," Applied Optics, Vol. 33, No.20, pp.4497-4500 (1994)

[61] Marvin A. Schofield and Yimei Zhu, "Fast phase unwrapping algorithm for interferometric applications," Optics Letters, Vol. 28, No. 14, pp.1194-1196 (2003)

[62] Mingquan Bao, Leong Keong Kwoh and Kuldip Singh, "An Improved Least-Squares Method for INSAR Phase Unwrapping," IEEE, pp.62-64 (1998)

[63] Hua Lu, Chao-pin Yeh and Jiabin Dai, "Experimental Evaluation of Effect of Global to Local Interaction on HDI Solder Joint Deformation," IEEE, *Electronic Components and Technology Conference*, pp.469-475 (1999)

[64] Rafael C. Gonzalez, Richard E. Woods, "Digital image processing (2nd Edition)," by Prentice Hall, pp. 233-238, 520-554, 572-600 (2002)

[65] Peter C. Gasson, "Geometry of spatial forms," (1983)

[66] Q. Hu, P. S. Huang, Q. Fu, and F. P. Chiang, "Calibration of a 3-D shape measurement system," Opt. Eng. Vol. 42, pp. 487-493 (2003)

APPENDIX 1

Program flow chart

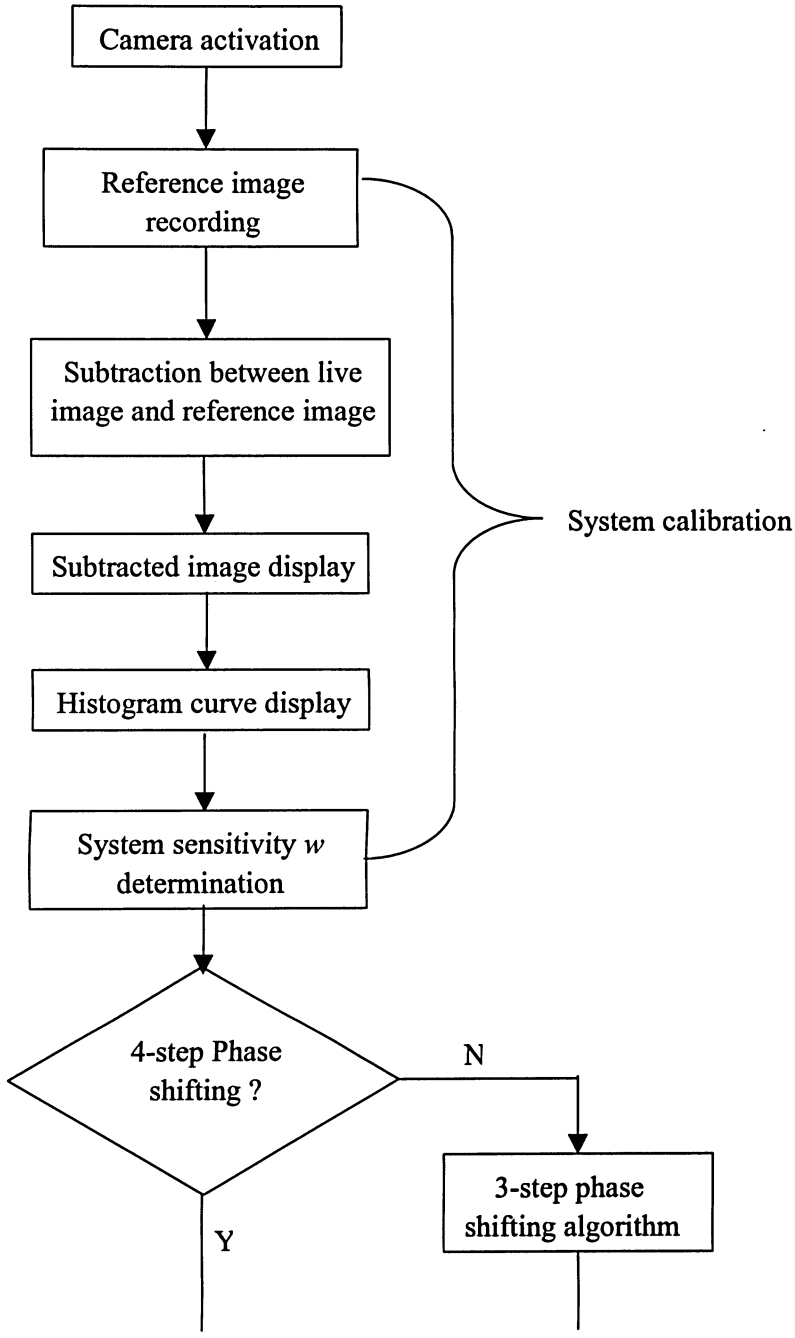

Fig. A-1 Program flow chart of the modified shadow moiré technique.

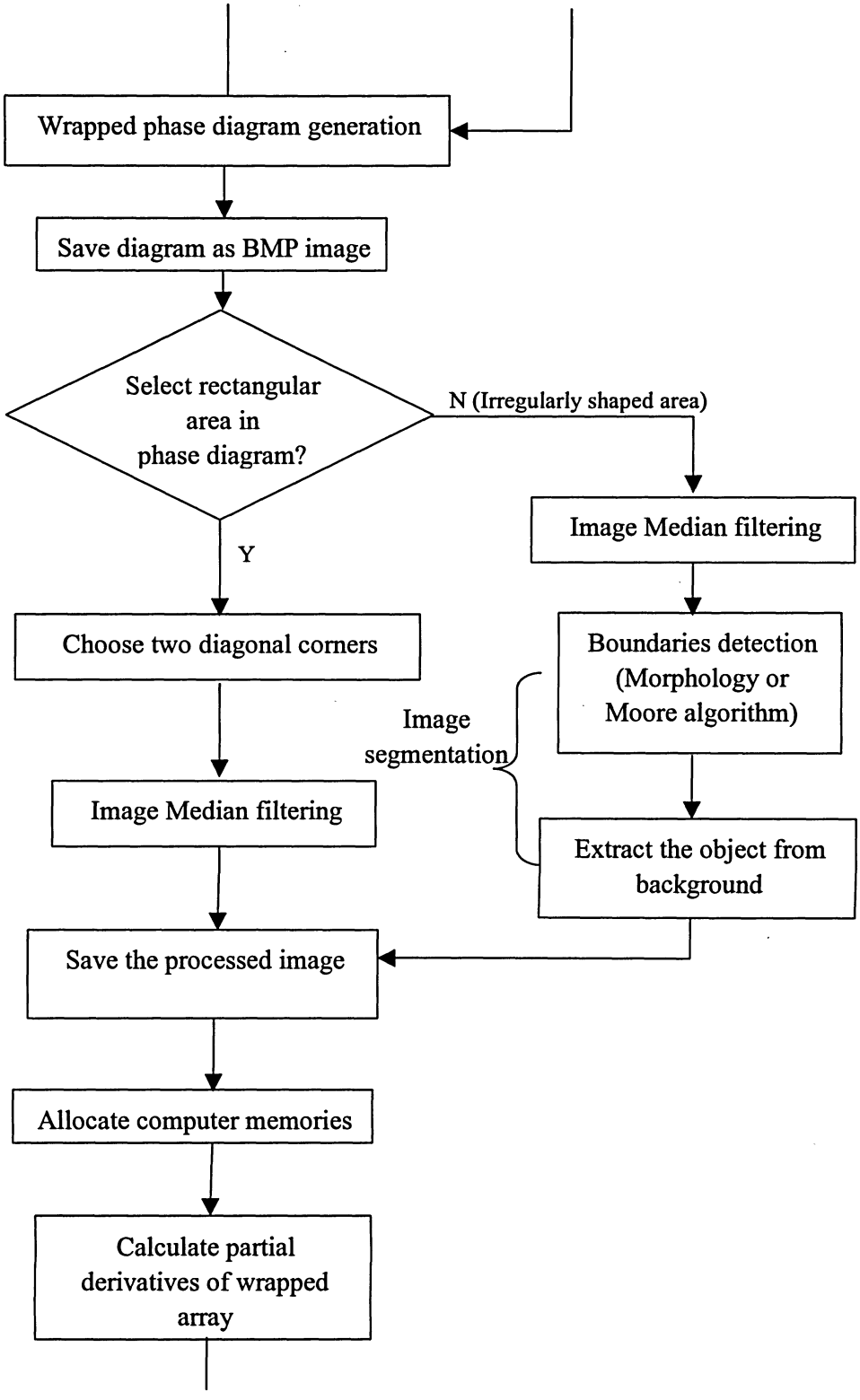

Fig. A-1 (continued).

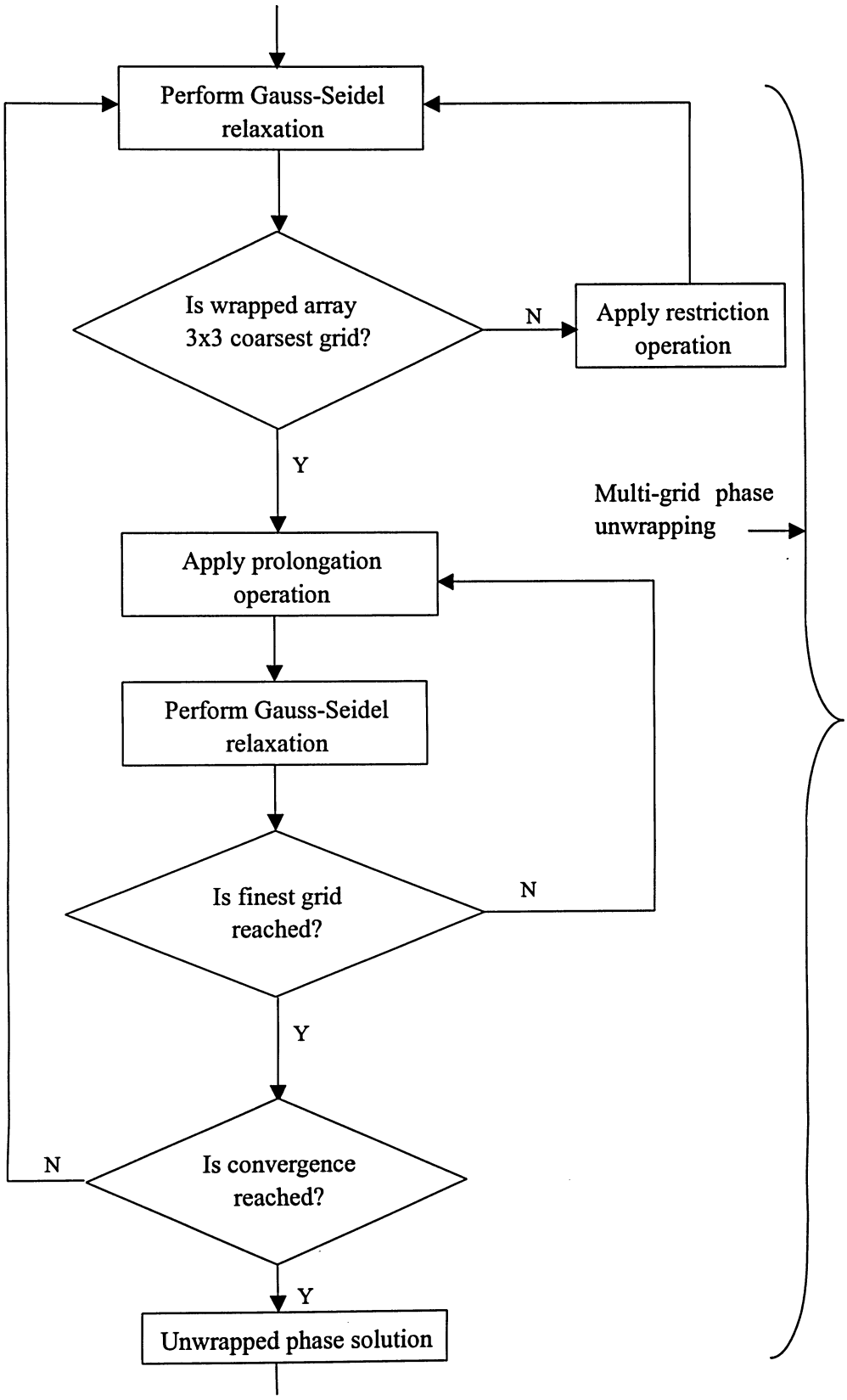

Fig. A-1 (continued).

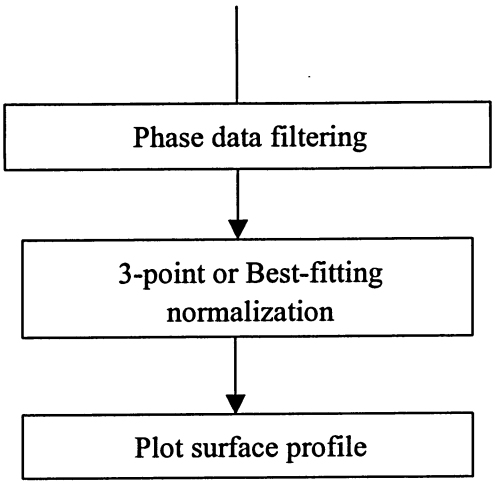

Fig. A-1 (continued).

APPENDIX 2

Warpage results of electronic components

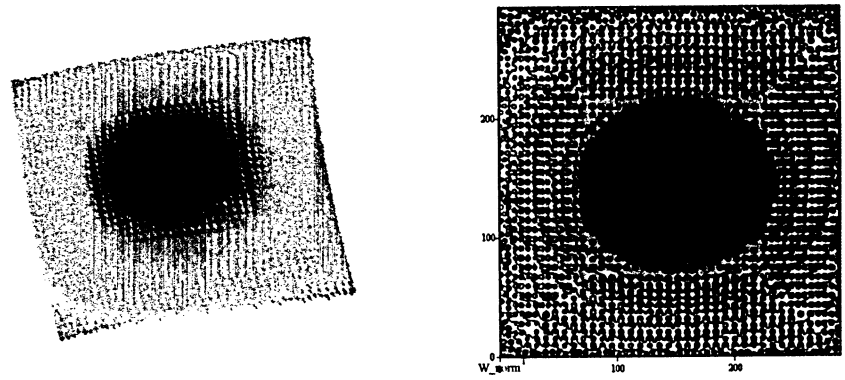

Fig. A-2 (a) Warpage of a PBGA at room temperature.

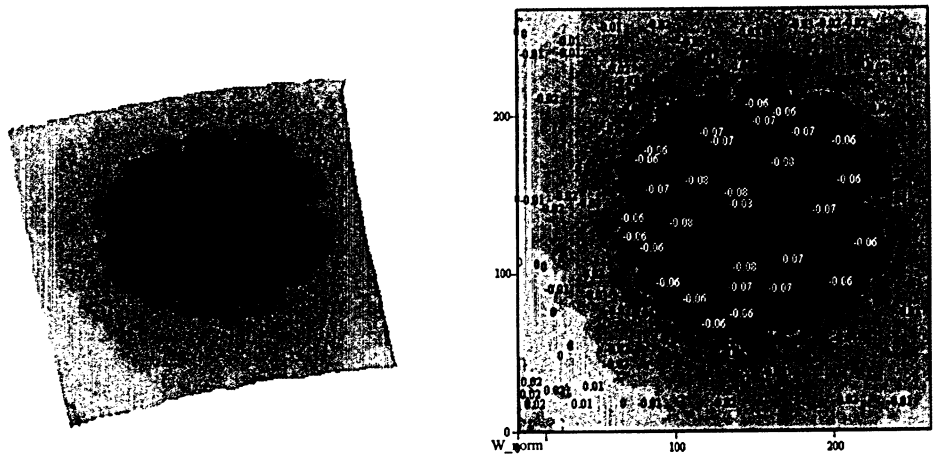

Fig. A-2 (b) Warpage of a PCBA at room temperature.

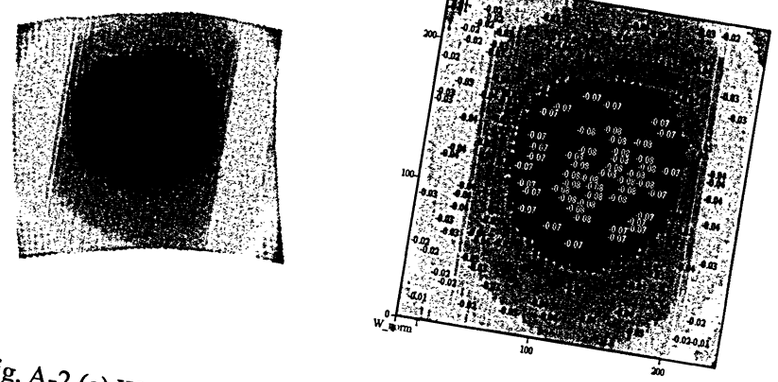

Fig. A-2 (c) Warpage of a CBGA at room temperature.